Journal Pre-proof

Preparation of a novel metallothionein-AuNP composite material by genetic modification and Au-S covalent combination

Xuefen Li, Hui Liu, Yuxia Wang, M. James C. Crabbe, Lan Wang, Wenli Ma, Zhumei Ren

PII: S0141-8130(24)00763-3

DOI: https://doi.org/10.1016/j.ijbiomac.2024.129960

Reference: BIOMAC 129960

To appear in: *International Journal of Biological Macromolecules*

Received date: 12 October 2023

Revised date: 22 January 2024

Accepted date: 1 February 2024

Please cite this article as: X. Li, H. Liu, Y. Wang, et al., Preparation of a novel metallothionein-AuNP composite material by genetic modification and Au-S covalent combination, *International Journal of Biological Macromolecules* (2023), https://doi.org/10.1016/j.ijbiomac.2024.129960

This is a PDF file of an article that has undergone enhancements after acceptance, such as the addition of a cover page and metadata, and formatting for readability, but it is not yet the definitive version of record. This version will undergo additional copyediting, typesetting and review before it is published in its final form, but we are providing this version to give early visibility of the article. Please note that, during the production process, errors may be discovered which could affect the content, and all legal disclaimers that apply to the journal pertain.

© 2024 Published by Elsevier B.V.

Preparation of a novel metallothionein-AuNP composite material by genetic modification and Au-S covalent combination

Xuefen Li[a], Hui Liu[a], Yuxia Wang[a], M. James C. Crabbe[a,b,c], Lan Wang[a], Wenli Ma[a,*], Zhumei Ren[a,*]

[a] School of Life Science, Shanxi University, Taiyuan 030006, PR China

[b] Wolfson College, University of Oxford, Oxford OX2 6UD, UK

[c] Institute of Biomedical and Environmental Science & Technology, School of Life Sciences, Faculty of Creative Arts, Technologies and Science, University of Bedfordshire, University Square, Luton LU1 3JU, UK

*Corresponding authors.

Postal address: School of Life Science, Shanxi University, No. 92, Wucheng Road, Taiyuan 030006, PR China

E-mail address: mawl@sxu.edu.cn, zmren@sxu.edu.cn

Abstract

Metallothionein (MTs) can be used in the prevention and treatment of tumors and diabetes due to its antioxidant properties. However, it is necessary to solve its non-transmembrane properties and further improve its antioxidant activity, increase its fluorescence visualization and enhance its stability to meet practical applications in the biomedical field. Here, we report the preparation of a novel metallothionein-AuNP composite material with high transmembrane ability, fluorescence visualization, antioxidant activity, and stability by genetic modification (introducing transduction peptide TAT, fluorescence tag GFP and increasing sulfydryl groups) and immobilization technology (covalently bonding with AuNPs). The transmembrane activity of modified proteins was verified by immunofluorescence. Increasing the sulfhydryl content within a certain range

Journal Pre-proof

can enhance the antioxidant activity of the protein. In addition, GFP were used to further simplify the imaging of the metallothionein-AuNP composite in cells. XPS results indicated that AuNPs can immobilize metallothionein through Au-S covalent bonds. TGA characterization and degradation experiments showed that thermal and degradation stability of the immobilized material was significantly improved. This work provides new ideas to construct metallothionein composites with high transmembrane ability, antioxidant activity, fluorescence visualization and stability to meet novel applications in the biomedical field.

Graphical Abstract

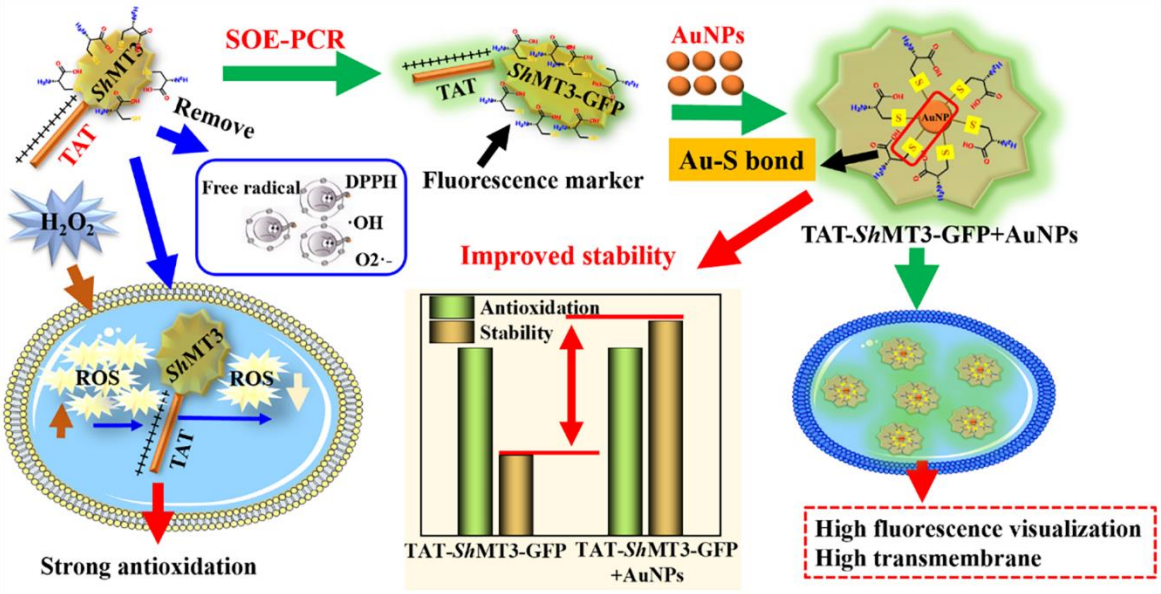

Keywords: TAT-protein transduction peptide; Modified proteins; Antioxidant; GFP-fluorescent tag; AuNPs; Stability

1. Introduction

Metallothionein (MTs) are a class of non-transmembrane activity proteins widely present in organisms, containing about 50-80 amino acids, with molecular weights about 6-10 KDa; Cysteine (Cys-) accounts for 23%-33% of the amino acid composition [1]. Due to the presence

of large amount of Cys-, MTs are endowed with special physiological functions, including heavy metal detoxification [2], participating in the balance of essential metal elements in the body [3] and scavenging free radicals [4-6]. In addition, some studies have also shown that MTs play an important role in tumorigenesis and the prevention and treatment of diabetes due to their strong antioxidant function [7-8].

The modification of gene sequences at the molecular level by targeted mutagenesis to obtain functionally enhanced proteins is a common means of protein modification [9-12]. In our previous studies, the full-length cDNA of *Sinopotamon henanense* metallothionein (*Sh*MT) has been cloned, three modified proteins of *Sh*MT were obtained by targeted mutagenesis, and the most powerful modified protein with heavy metal binding ability was screened [13-14]. However, the exogenous antioxidant properties of the modified proteins and their intracellular antioxidant activity have not been studied.

Moreover, although the modified proteins obtained belongs to functional proteins, their poor stability limits practical application [15]. Immobilization is a convenient method to improve the stability of biological macromolecules, by chemical, physical or biological means to immobilize free microorganisms on a carrier to improve their stability [16-17].

As an immobilized carrier, nanogolds (AuNPs) has been widely researched, developed and applied in many directions such as sensing, catalysis and medical because of its various physicochemical properties, including good stability from gold, biocompatibility and unique easily modifiable properties from its nanometer size [18-19]. The sulfhydryl molecule forms stable gold-sulfur (Au-S) covalent bonds with gold atoms on the surface of gold nanoparticles, forming functionalized materials for imaging [20], carrier delivery [21-22] and other biomedical fields [23]. Metallothionein contains a large number of cysteine residues (Cys-), which provides

a carrier basis for the formation of Au-S [24]. The combined application of metallothionein and AuNPs has been reported in the literature, including POSS polymer-caged AuNPs for sensitive colorimetric detection of metallothionein [25], development of gold nanoparticle immobilized metallothionein sensors [26], and L-cystine encapsulated AuNPs which were analyzed for toxicity and antioxidant properties [27].

In this study, we introduced the transduction peptide TAT by long primer PCR based on the three modified proteins obtained in our previous work to investigate the effect of cysteine content on the intracellular antioxidant activity of the modified proteins and their mechanism of action [28-29]. The fluorescence visualization was achieved by introducing GFP fluorescence tag. In addition, AuNPs was introduced as an immobilized carrier to increase the stability of the modified proteins. SEM, TEM, XPS and antibacterial assays were used to verify the binding of AuNPs and modified proteins. The transmembrane ability, antioxidant activity and stability of AuNPs/modified protein composites were investigated. Finally, a novel composite material with high transmembrane ability, antioxidant activity, fluorescence visualization and stability was prepared. which provides new ideas for further applications of metallothionein.

2. Materials and methods

2.1. Experimental materials and reagents

The experimental reagents and purchasing manufacturers involved in this study are presented in detail in TEXT S1.

2.2 Vector construction, protein expression purification and validation

The prokaryotic expression vector pET28a-SUMO-*Sh*MT had been constructed previously [15], and mutant expression vectors pET28a-SUMO-*Sh*MT1, pET28a-SUMO-*Sh*MT2 and

pET28a-SUMO-*Sh*MT3 were obtained by site-directed mutagenesis [13]. In this study, primers fused with TAT-Core sequence (TATGGCAGGAAGAAGCGTAGACAGAGACGTAGA) were designed and the target fragments were amplified with pET28a-SUMO-*Sh*MT, pET28a-SUMO-*Sh*MT1, pET28a- SUMO-*Sh*MT2 and pET28a-SUMO-*Sh*MT3 as templates and recover the gene fragments *TAT-ShMT*, *TAT-ShMT1*, *TAT-ShMT2* and *TAT-ShMT3*. The expression vector (pET28a-) was obtained by double enzyme digestion (*Bam*H I and *Hin*d III). Finally, the recovered gene fragments and the digested expression vector were connected by T4-DNA ligase to obtain prokaryotic expression vectors pET28a-TAT-*Sh*MT, pET28a-TAT-*Sh*MT1, pET28a-TAT-*Sh*MT2 and pET28a-TAT-*Sh*MT3 and then sequenced. Primer design is shown in Tab. S1.

The sequenced recombinant plasmids pET28a-TAT-*Sh*MT, pET28a-TAT-*Sh*MT1, pET28a-TAT-*Sh*MT2, and pET28a-TAT-*Sh*MT3 were transformed into *E. coli* BL21(DE3) competent cells to express the target proteins (TAT-*Sh*MT, TAT-*Sh*MT1, TAT-*Sh*MT2, TAT-*Sh*MT3). The transformants were grown in 500 mL LB liquid medium with a final concentration of 50 μg/mL Kana at 37°C. When the OD_{600} reached 0.5, the proteins were induced by adding 1.0 mM IPTG to the medium and cells cultured at 37°C for 8 h. Cells were collected by centrifugation (20 min, 8,000 g, 4°C) and lysed by ultrasonication in five volumes (v/w) of lysis buffer (20 mM Tris-HCl, pH 7.8, 0.2 mM PMSF, and 0.1% Triton). When the bacterial solutions were relatively transparent, it was taken that the cells had been lysed. After centrifugation of the cell lysate at 8,000 g for 30 min, the supernatants were recovered. The expression of target proteins was detected by SDS-PAGE.

Supernatants were then loaded onto a HisTrip column (Ni-NTA), after removing other proteins with 20 mM imidazole, then were eluted with sequential 500 mM imidazole buffers.

Journal Pre-proof

SDS-PAGE was used to detect the proteins in the eluent. The eluate containing the target proteins was collected, the remaining imidazole and NaCl was removed by ultrafiltration, the protein concentration was determined, then stored at -80°C.

Since the exogenous proteins by induced expression in *E. coli* BL21 competent cells through the prokaryotic expression vector pET28a-, pET28a- contains 6-His tag, so the proteins (TAT-*Sh*MT, TAT-*Sh*MT1, TAT-*Sh*MT2, TAT-*Sh*MT3) contain 6-His tag, and based on this feature, these proteins were verified by Western blot experiments (Mouse anti His-Tag mAb as the primary antibody and Goat Anti Mouse IgG H&L as the secondary antibody).

Fourier transformation infrared spectroscopy (FT-IR) analysis can predict whether the secondary structure of different modified proteins changes. 1.0 mg of freeze-dried protein powder was mixed with 100 mg of potassium bromide powder, pressed into tablets and analyzed by infrared spectrometer in the scanning spectral range of 500-4000 cm^{-1}.

2.3 In vitro antioxidant assay of recombinant fusion proteins

The in *vitro* antioxidant activity of the modified proteins was evaluated by measuring the scavenging rate of DPPH free radical, hydroxyl radical (·OH), superoxide anion ($O2\cdot^{-}$) and total antioxidant capacity (Tac) of the modified proteins. Specific steps are shown in TEXT S2.

2.4 The transmembrane ability of proteins was detected by immunofluorescence

293T cells grown to 3-4 generations were collected. The cells were resuspended in 1.0×10^{3}/well cells, spread on the climbing piece in the 6-well plate and cultured overnight. After the culture, the cells were washed three times with sterile PBS, and purified protein (final concentration 100 μg/mL) was mixed with 2 mL medium, and then added to the six-well plate to continue culturing the cells for 24 h. The medium was removed, the cells were washed with PBS three times, and paraformaldehyde added to fix the cells for 20 min. After fixation, 0.1% Triton

X-100 was used for penetration about 20 min. Finally, it was sealed with 5% BSA and allowed to stand at room temperature for 1 h.

The primary-anti Mouse anti His-Tag mAb was diluted with 5% BSA in the ratio of 1:50, and 20 μL was added to each tablet, and incubated at 4 ℃ overnight. The secondary-anti Goat Anti Mouse lgG H&L (100 μL/well) was diluted with 5% BSA in the ratio of 1:1000, dark operation. After the secondary-antibody was added, incubation proceeded at room temperature for 1.5 h. After washing with PBS for 3 times, the climbing plates were taken out and placed on glass slides, dropping 10 μg/mL DAPI working fluid (100 μL/well) in the climbing tablet center, and adding anti-fluorescence quencher (50 μL/well) to each slide to prevent fluorescence quenching. Finally, they were observed and photographed with a fluorescence microscope in the dark.

2.5 Establishment of H_2O_2-induced oxidative damage model and cytotoxicity of four proteins on 293T cells

293T cells grown to 3-4 generations were treated in 96-well plates with different concentrations of H_2O_2 for 3 h to determine the H_2O_2 concentration required to reduce the cell viability of 293T cells to 50%. After incubation, the cells were washed with PBS 3 times, and the cell viability was measured by the cck8 test kit.

Toxic effects of four proteins (TAT-*Sh*MT, TAT-*Sh*MT1, TAT-*Sh*MT2, TAT-*Sh*MT3) at concentrations of 0, 50, 100, 200, 400, 800 μg/mL were measured using the same method on cells. Further determination of the repair effect of proteins on cellular oxidative damage used the same method.

2.6 Effect of proteins on 293T cells apoptosis under oxidative stress

The 293T cells were seeded in 6-well plates at a cell density of 1.0×10^6/well for 24 h. After

incubation, the cells were washed 3 times with PBS, and treated with the optimal concentration of proteins in the medium for 24 h. After washing the cells with PBS, the cells were incubated with H_2O_2 in the medium for 3 h. Cells were harvested by trypsinization and washed 3 times with PBS. 200 μL Annexin V-FITC binding solution was added to resuspend the cells, and then 5 μL Annexin V-FITC staining solution was added. The mixture was incubated on ice for 30 min in the dark. 10 μL PI was added before putting on the machine and incubated on ice for 5 min in the dark. Then 200 μL PBS was added and mixed, and it was immediately tested on the Flow Cytometer.

2.7 ROS determination and Caspase-3 and -9 activities in different groups

Intracellular ROS levels were assessed using a DCFH-DA (2,7-Dichlorofuorescin Diacetate) assay. The 293T cells were seeded in 96-well about 1.0×10^5 cells/well and cultured for 24 h. After incubation, the cells were washed three times with PBS and treated for 24 h in the medium with the optimal concentration of proteins. After processing, the cells were incubated with H_2O_2 in the medium for 3 h. Then, the cells were washed three times with PBS, and pre-treated with 10 μmol/L of DCFH-DA in media at 37◦C for 20 min. Finally, cells were washed 3 times with PBS and ROS levels (fluorescence intensity) were measured by a Microplate Reader at excitation and emission wavelengths of 488 and 525 nm, respectively.

Total RNA in cells of different treatment groups was extracted using the TRNzol reagent. Reverse transcription of mRNA into cDNA used the Reverse transcription kit. q-PCR used the Real time fluorescence quantitative PCR kit. q-PCR analysis was performed three times. The primer sequences are listed in Tab. S2.

To evaluate the effects of TAT-*Sh*MT3 on Caspase-3 and-9 activities in 293T cells, the 293T cells were seeded in 6-well plates with 1.0×10^5 cells/well for 24 h. The enzyme activity test kit

Journal Pre-proof

was used to measure and calculate the activities of Caspase-3 and Caspase-9 in different treatment groups.

2.8 Construction of GFP fusion vector by SOE-PCR

Based on the principle of overlapping extension PCR (SOE-PCR), two pairs of primers containing overlapping fragments were designed, primer design is shown in Tab. S3. The successfully sequenced prokaryotic expression vector pET28a-TAT-*Sh*MT3 and *GFP* gene segment was were used as a template to construct overlapping fragments using a three-step PCR method. A recombinant expression vector was constructed through double enzyme digestion for subsequent protein expression.

2.9 Protein expression and validation of its binding with AuNPs

The sequenced recombinant plasmids pET28a-TAT-*Sh*MT3-GFP were transformed into *E. coli* BL21(DE3) competent cells to express the target proteins TAT-*Sh*MT3-GFP. For protein expression and purification steps refer to section 2.2.

To couple proteins to AuNPs, the citrate solution of AuNPs was adjusted to pH 8.5. Then, TAT-*Sh*MT3-GFP was added to AuNPs until the final concentration was 20 μg/mL and gently shaken at 4℃. The supernatant was collected by centrifugation, and the binding efficiency was further verified by SDS-PAGE.

After culturing 4 groups of 50 mL empty *E. coli* to an OD600 value of 0.5. The first group was a blank treatment group, the second group was an AuNPs treatment group, the third group was a TAT-*Sh*MT3-GFP treatment group, and the fourth group was a TAT-*Sh*MT3-GFP+AuNPs treatment group, so that their final concentrations were all 20 μg/mL. The binding of TAT-*Sh*MT3-GFP with AuNPs was verified by growth curve and plate antibacterial experiments.

The binding of TAT-*Sh*MT3-GFP and AuNPs was further verified by SEM (SEM, TESCAN

MIRA4), TEM (TEM, FEI Talos F200S), and XPS (XPS, Thermo Scientific ESCALAB 250Xi).

2.10 Transmembrane validation

Cells from different treatment groups were fixed (Refer to 2.4). Since GFP is a green fluorescent tag, it can be verified by dropping it directly into different treatment groups for transmembrane. This was performed by co-incubation of proteins and cells, removing the climbing plates and placing them on glass slides, dropping 10 μg/mL DAPI working solution (100 μL/well) into the center of the climbing plates, and adding anti-fluorescence bursting agent (50 μL/well) to each slide to prevent fluorescence bursting. Finally, they were observed and photographed in the dark with a fluorescence microscope. Cells were collected and fluorescence intensity was measured by Microplate Reader.

Cell membrane integrity after TAT-*Sh*MT3-GFP+AuNPs treatment was verified using a lactate dehydrogenase (LDH) assay. And the cells of the treated group were fixed to verify the time of entry of TAT-*Sh*MT3-GFP+AuNPs into the cells in as well as the localization in cells.

2.11 Cytotoxicity and ROS determination

The cytotoxicity of different treatment groups was determined by cck8 assay.

Intracellular ROS levels were determined using a DCFH-DA (2,7-Dichlorofuorescin Diacetate) assay.

2.12 Stability analysis

Protein degradation stability of TAT-*Sh*MT3-GFP and binding product (TAT-*Sh*MT3-GFP+AuNPs) was measured by BCA protein concentration assay, and thermal stability of TAT-*Sh*MT3-GFP and TAT-*Sh*MT3-GFP+AuNPs was measured by thermogravimetry. Note: The references to TAT-*Sh*MT3-GFP+AuNPs in the following text refer to the binding products of TAT-*Sh*MT3-GFP and AuNPs.

Journal Pre-proof

2.13 Statistical method

All experiments were repeated at least three times, and the data used in the analysis of the results were the Mean (Mean) ± Standard Deviation (SD) (M ± SD). Statistical analysis was performed using SPSS 25.0 software. Origin 2022 was used for plotting. One-way analysis of variance ANOVA was used to analyze the differences between the control and experimental groups. $p < 0.05$ means significant, $p < 0.01$ means very significant.

3. Results and Discussion

3.1 Vector construction, protein expression purification and validation

The electrophoresis detection results of the gene amplification products showed that the target fragments *TAT-ShMT*, T*AT-ShMT1*, *TAT-ShMT2*, and *TAT-ShMT3* with *Bam*H I and *Hin*d III restriction endonuclease sites of 238bp in size were successfully obtained (Fig. 1A). Similarly, the pET28a- vector was also digested with two endonucleases, *Bam*H I and *Hin*d III (Fig. 1B). The amplified fragments were linked with the digested expression vector pET28a- through T_4-DNA-Ligase to obtain four expression vectors: pET28a-TAT-*Sh*MT, pET28a-TAT-*Sh*MT1, pET28a-TAT-*Sh*MT2, pET28a-TAT-*Sh*MT3, and they were sequenced. The sequencing results showed that all four expression vectors were successfully constructed (Fig. S1).

After successfully constructing four expression vectors pET28a-TAT-*Sh*MT, pET28a-TAT-*Sh*MT1, pET28a-TAT-*Sh*MT2, pET28a-TAT-*Sh*MT) were transformed into *E. coli* BL21 (DE3) competent cells, inducing expression of the target proteins, and further purified through nickel column chromatography. SDS-PAGE results showed that the four proteins (Fig. 1C (Lane 2, Lane 4, Lane 6, Lane 8)) were abundantly expressed after induction with 1 mM IPTG at 37°C and 180 rpm for 8 h. The protein expression results also showed that the proteins

Journal Pre-proof

could not be expressed without IPTG induction in consistent bacterial concentration, time and temperature (Fig. 1C (Lane 1, Lane 3, Lane 5, Lane 7)) [30-32.]. In order to obtain the target protein, the crude protein solution was purified. Since the vector contained 6-His-tag, the recombinant proteins containing 6-His-tag obtained by expression can bind to nickel and elute by competition of imidazole [33-34]. The results showed that 500 mM of imidazole was able to elute the target protein to obtain pure protein for subsequent experiments (Fig. 1D (Lane 3, Lane 6, Lane 9, Lane 12)).

Since the purified proteins TAT-*Sh*MT, TAT-*Sh*MT1, TAT-*Sh*MT2, and TAT-*Sh*MT3 all contain 6-His-tag, we chose Mouse anti His-Tag mAb as the primary antibody and Goat anti-Mouse IgG H&L as the secondary antibody by Western blot experiment to direct detection. The results showed a stable dimer at about 20 KDa and a small amount of monomer at about 10 KDa (Fig. 1E). This result indicated that TAT-*Sh*MT, TAT-*Sh*MT1, TAT-*Sh*MT2, and TAT-*Sh*MT3 proteins mainly exist in the form of dimers, which was in agreement with the previous study [13]. Therefore, in the process of subsequent functional validation, all the proteins obtained by our purification were dimers.

In order to determine whether the secondary structure of the modified proteins had changed, we carried out Fourier ransformation infrared spectroscopy (FT-IR) analysis [35-38]. The infrared spectra of the three standard amide bands are a powerful basis for analyzing the secondary structure of proteins [39-40]. The spectrum of amide I band appeared around 1700-1600 cm^{-1} (mainly C=O stretch), the spectrum of amide II band appeared around 1600-1500 cm^{-1} (C=N stretch and N-H bending vibration), and the spectrum of amide III band appeared around 1330-1220 cm^{-1} (N-H bending and C-N stretching vibration) [41-42]. As shown in Fig. 1F, FT-IR was performed using four proteins of the same concentration, the mid-infrared

Journal Pre-proof

spectra (400-4000 cm^{-1}) of the four proteins (TAT-*Sh*MT, TAT-*Sh*MT1, TAT-*Sh*MT2, TAT-*Sh*MT3) were very similar. The characteristic absorption peak with an absorption frequency of 1624 cm^{-1} represents a β-fold in the amide I band [43, 14]. The characteristic absorption peak with an absorption frequency of 1225 cm^{-1} represents a β-fold in the amide III band [38]. In the spectrogram, no peak corresponding to the amide II band was found, probably because the peak of the amide II band is prone to shift, so most studies on the secondary structure focus on the amide I and amide III bands [37]. The four proteins showed almost identical O-H absorption peaks at 3298 cm^{-1} [38]. The above results show that although the primary structures of the four proteins were changed, the secondary structures did not change. It is noteworthy that the stretching strength of the S-H absorption peak at 2355 cm^{-1} in the four proteins had changed, and the absorption strength shows the following trend: TAT-*Sh*MT3 > TAT-*Sh*MT2 > TAT-*Sh*MT1 > TAT-*Sh*MT, which is due to the different cysteine content in the four proteins, resulting in different S-H content [14, 44]. The amide I and amide III bands of these four proteins exhibited peak shapes consistent with previous work, confirming the presence of metallothionein [14].

Journal Pre-proof

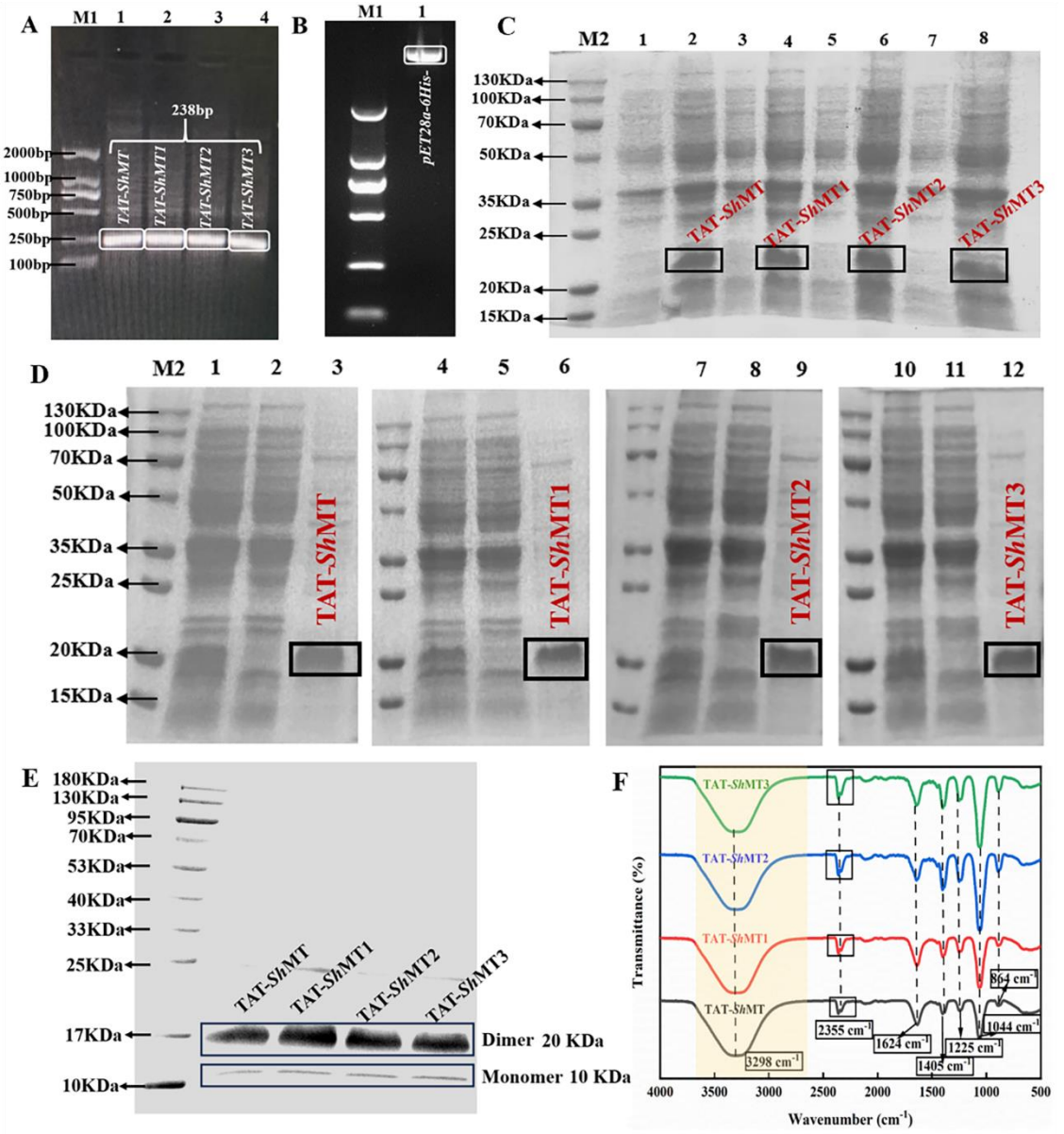

Fig. 1. Vector construction, protein expression purification and FT-IR validation. (A) PCR amplification of *TAT-ShMT*、*TAT-ShMT1*、*TAT-ShMT2*、*TAT-ShMT3* gene fragments. M1: DL2000 DNA marker; Lane 1-4: Gene segments (*TAT-ShMT*, *TAT-ShMT1*, *TAT-ShMT2*, *TAT-ShMT3*). (B) The double digestion of *pET28a-*. (C) SDS-PAGE analysis of four recombinant fusion proteins (TAT-*Sh*MT, TAT-*Sh*MT1, TAT-*Sh*MT2, TAT-*Sh*MT3) expression. M2: Protein marker; Lane 1, 3, 5, 7: Uninduced; Lane 2, 4, 6, 8: Induced. (D) SDS-PAGE analysis of four recombinant fusion

proteins (TAT-*Sh*MT, TAT-*Sh*MT1, TAT-*Sh*MT2, TAT-*Sh*MT3) purification. Lane 1, 4, 7, 10: Cell extract supernatants; Lane 2, 5, 8, 11: Protein penetration; Lane 3, 6, 9, 12: Protein purification solutions. (E) Verification of proteins expression by Western blot. (F) The four proteins analyzed by FT-IR in the scanning band of 500-4000 cm^{-1}.

3.2 In vitro antioxidant assay of recombinant fusion proteins

According to the literatures, the antioxidant activity of exogenous antioxidants is usually measured according to the free radical scavenging ability [45-46]. Thus, according to the steps of the DPPH, ·OH, O2·- Assay Kit, the scavenging ability of four proteins (TAT-*Sh*MT, TAT-*Sh*MT1, TAT-*Sh*MT2, TAT-*Sh*MT3) on DPPH, ·OH and $O2^{\cdot-}$ free radicals were measured. The results showed that four proteins had relatively high scavenging ability to DPPH, ·OH and $O2^{\cdot-}$; the scavenging ability increased with the increase of protein concentration, and tended to stabilize (Fig. 2A, B, C). Similarly, the total antioxidant capacity of the four proteins showed a similar trend: TAT-*Sh*MT3 > TAT-*Sh*MT2 > TAT-*Sh*MT1 > TAT-*Sh*MT (Fig. 2D). The above results suggest that the relative antioxidant capacity of the modified proteins increases with increasing cysteine content. The linear regression calculation is shown in Fig. S2, and the calculation of IC_{50} value further supports this conclusion (Tab. S4).

Journal Pre-proof

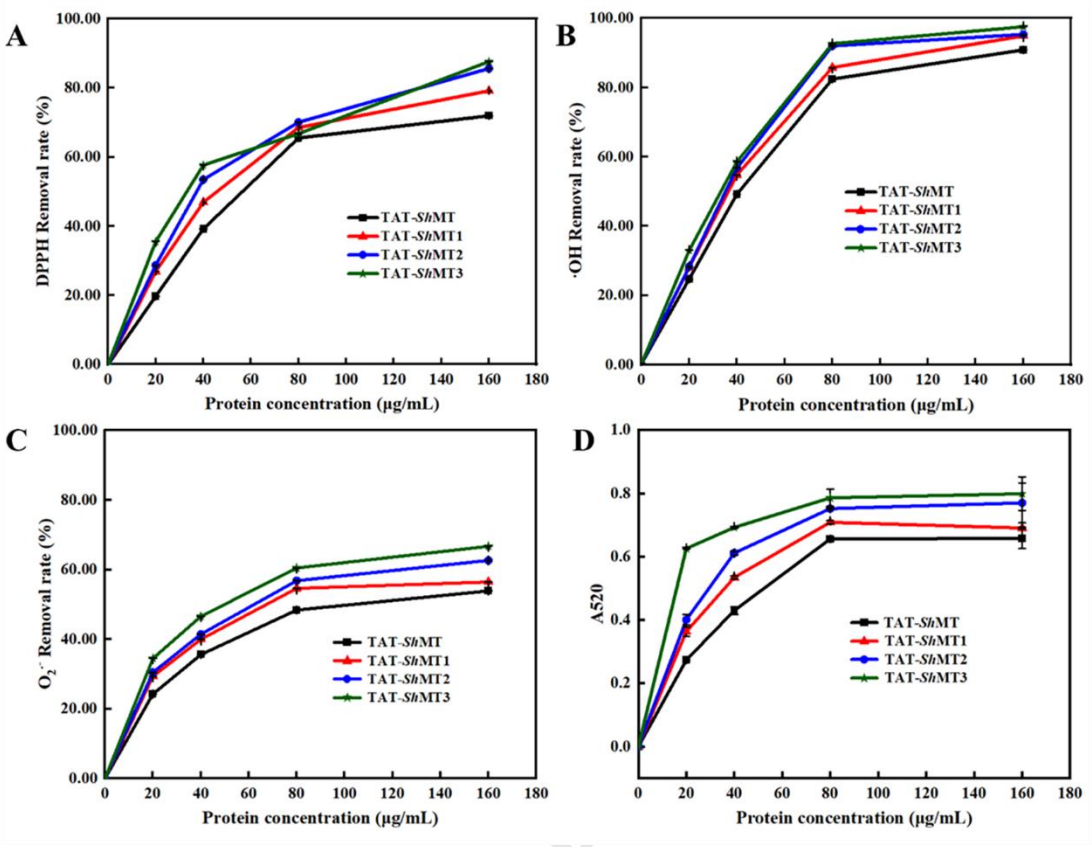

Fig. 2. Determination of in *vitro* antioxidant activity of different proteins. (A) Clearance rate of DPPH by TAT-*Sh*MT1/2/3. (B) Clearance rate of ·OH by TAT- TAT-*Sh*MT1/2/3. (C) Clearance rate of O2·- by TAT-*Sh*MT1/2/3. (D) Determination of total antioxidant capacity by TAT-*Sh*MT1/2/3.

3.3 The transmembrane ability of proteins was detected by immunofluorescence

Firstly, bioinformatics was used to predict the transmembrane results of proteins without and with TAT. The results showed that proteins without TAT indicated “outside”, while proteins with TAT indicated “inside” (Fig. S3).

Immunofluorescence is a technique for antigen cell localization by labeling antibodies with fluorescent substances [47]. Four recombinant proteins TAT-*Sh*MT, TAT-*Sh*MT1, TAT-*Sh*MT2 and TAT-*Sh*MT3 were added to 293T cells for coincubation for 24 h. Whether the recombinant

proteins could enter the cells was observed by immunofluorescence. The results showed that the four proteins fused with transmembrane peptide TAT could enter the cells. It can be seen from Fig. 3A that the protein TAT-*Sh*MT with membrane penetrating peptide could enter the cell, while the protein *Sh*MT without membrane penetrating peptide could not enter the cells. Similar results were obtained with TAT-*Sh*MT1, TAT-*Sh*MT2 and TAT-*Sh*MT3 (Fig. 3B, C, D). The same results were obtained by observing at a higher resolution, that is, four proteins containing membrane penetrating peptides could enter 293T cells (Fig. 3E). In order to verify the transmembrane ability of proteins in different cells, H9c2 cells were used for further verification under the same conditions. The results showed that H9c2 cells also had high transmembrane ability (Fig. 3F) (Fig. 3A, B, C, D showed an objective lens 4x and a resolution of 200 μm; Fig. 3E, F showed an objective lens 40 x with a resolution of 50 μm). These results lay the foundation for further verification of the antioxidant activity of the proteins in cells. The specific steps for constructing control expression vector (pET28a-*Sh*MT, pET28a-*Sh*MT1, pET28a-*Sh*MT2, pET28a-*Sh*MT3), protein expression, and purification (*Sh*MT, *Sh*MT1, *Sh*MT2, *Sh*MT3) refer to section 2.2. The vector construction and protein expression results are shown in Fig. S4.

Journal Pre-proof

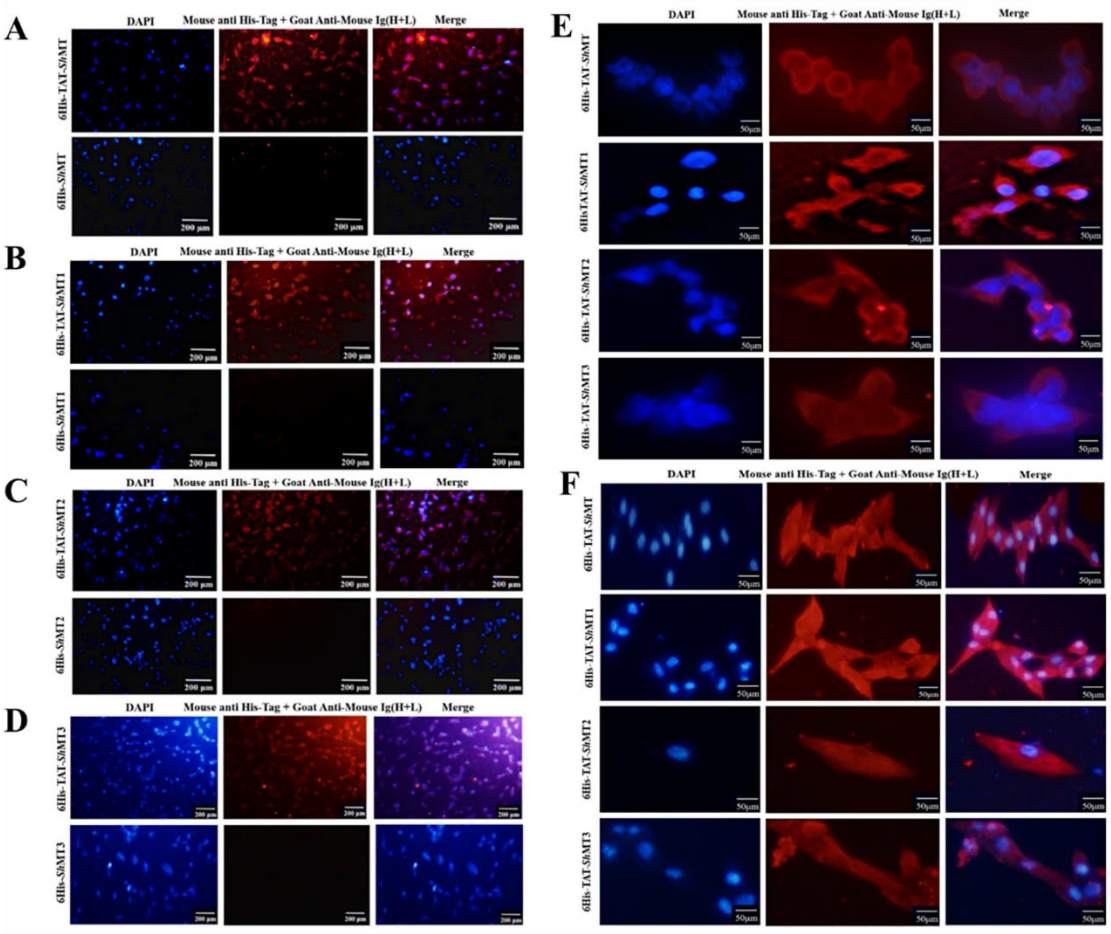

Fig. 3. Transmembrane effects of recombinant fusion proteins TAT-*Sh*MT, TAT-*Sh*MT1, TAT-*Sh*MT2, TAT-*Sh*MT3 by immunofluorescence.

3.4 Establishment of H_2O_2-induced oxidative damage model and Cytotoxicity of four proteins on 293T cells

In many studies on oxidative damage to cells, H_2O_2 is often used to establish cell oxidative damage model [48-49]. In order to obtain the H_2O_2 concentration when the cell viability decreased to about 50%, 293T cells were first treated with different concentrations of H_2O_2 (500, 1000, 2000, 4000, 8000 μmol/L). The results showed that when the H_2O_2 concentration was 1000 μmol/L, the cell viability was 60.20% ± 2.47%, and when the H_2O_2 concentration was 2000

μmol/L, the cell viability was 29.78 ± 3.00% (Fig. 4A). Therefore, the H_2O_2 concentration was further optimized between 1000-2000 μmol/L. As shown in Fig. 4B, when the H_2O_2 concentration was 1400 μmol/L, cell viability was 51.91% ± 1.48%, therefore, 1400 μmol/L-H_2O_2 concentration was determined to be the concentration that constructed the H_2O_2-induced oxidative damage model.

Four proteins (TAT-*Sh*MT, TAT-*Sh*MT1, TAT-*Sh*MT2, TAT-*Sh*MT3) were measured for cytotoxicity on 293T cells by a cck8 experiment. Effects of each protein on cell viability were measured at different concentrations (0, 50, 100, 200, 400 and 800 μg/mL). As can be seen from Fig. 4C, there was no significant difference in the cytotoxicity of the four proteins. When the protein concentration was less than 200 μg/mL, the four proteins showed no cytotoxicity ($p > 0.05$), all cell viability was above 95%. When the protein concentration reached 400 μg/mL, the cell viability decreased to 79.25% ± 5.33%, but when the protein concentration continued to increase to 800 μg/mL, the cell viability did not decrease significantly ($p > 0.05$). This result demonstrated that low concentration of proteins had no effect on cell viability, and high concentration proteins had little effect on cell viability. Therefore, in the following experiments, low concentrations of proteins were selected to further verify the protective effects on H_2O_2-induced oxidative damage in 293T cells.

Cells were pretreated with different concentrations of four proteins (0, 50, 100, 150, 200 μg/mL), and then treated with 1400 μmol/L H_2O_2 to prepare the H_2O_2-induced oxidative damage model. As shown in Fig. 4D, when treated with 1400 μmol/L H_2O_2 alone, the cell viability was about 50%. Furthermore, the cells were treated with 50 μg/mL proteins and then damaged with 1400 μmol/L H_2O_2, the results showed that the cell viability of the treatment groups (TAT-*Sh*MT1+1400 μmol/L H_2O_2, TAT-*Sh*MT2+1400 μmol/L H_2O_2, TAT-*Sh*MT3+1400 μmol/L

H_2O_2) all reached a significant level compared with the control group ($P < 0.05$). The cells were treated with 100 μg/mL proteins and then damaged with 1400 μmol/L H_2O_2, the results showed that the cell viability of the treatment group (TAT-*Sh*MT+1400 μmol/L H_2O_2) reached a significant level compared with the control group ($P < 0.05$), while the cell viability of the treatment groups (TAT-*Sh*MT1+1400 μmol/L H_2O_2, TAT-*Sh*MT2+1400 μmol/L H_2O_2, TAT-*Sh*MT3+1400 μmol/L H_2O_2) all reached a very significant level ($P < 0.01$) compared with the control group, and the order of cell viability was TAT-*Sh*MT3+1400 μmol/L H_2O_2 > TAT-*Sh*MT2+1400 μmol/L H_2O_2 > TAT-*Sh*MT1+1400 μmol/L H_2O_2 > TAT-*Sh*MT+1400 μmol/L H_2O_2. Subsequently, the results of cells treated with 150 and 200 μg/mL protein were not significantly different from those treated with 100 μg/mL, so 100 μg/mL proteins could be used as the optimal concentration. The results suggest that proteins protect 293T cells by preventing H_2O_2-induced oxidative stress and that TAT-*Sh*MT3 had the best protective effect, increasing cell viability by 30% compared to the control.

Journal Pre-proof

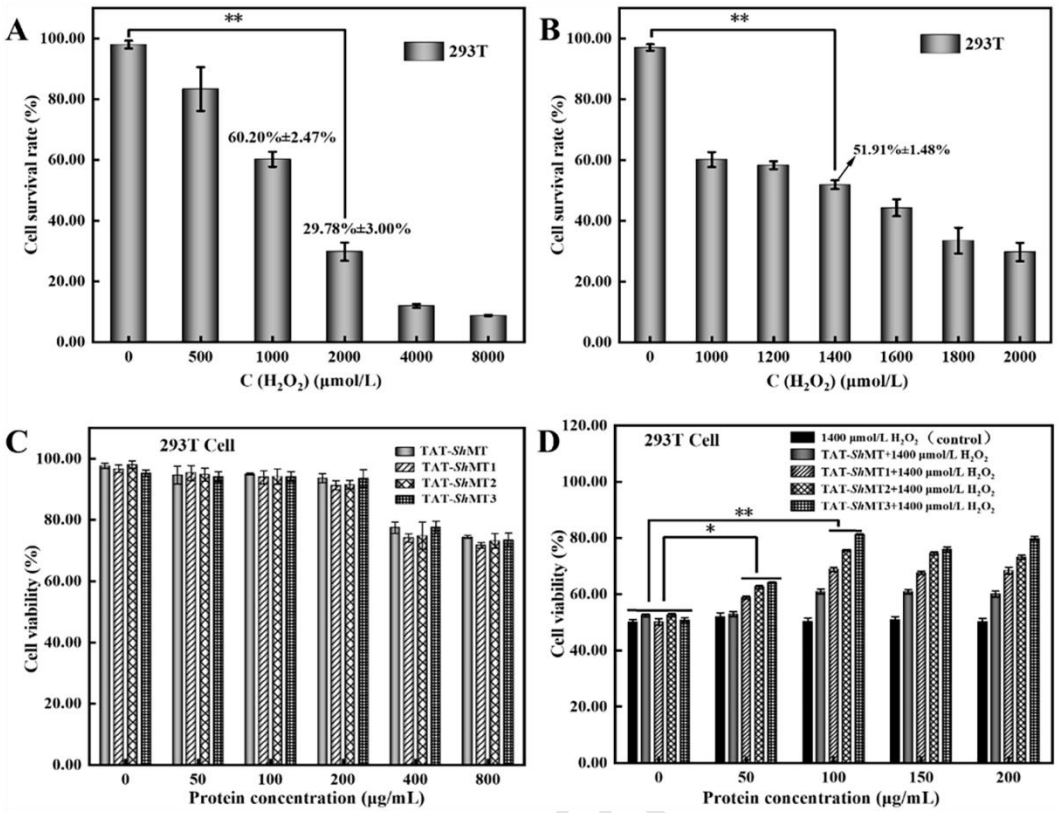

Fig. 4. (A, B) Establishment of oxidative damage model of hydrogen peroxide; (C) Cytotoxicity of four proteins with different concentrations to cells; (D) Repair effect of protein on oxidative damaged cells.

3.5 Effect of proteins on 293T cells apoptosis under oxidative stress

Flow cytometry can be used to determine the apoptosis rate of different treatment groups [50]. The Q1 quadrant represents the proportion of necrotic cells, the Q2 quadrant represents the proportion of late apoptotic cells, the Q3 quadrant represents the proportion of early apoptotic cells, and the Q4 quadrant represents the proportion of normal cells [51]. Therefore, the proportion of apoptotic cells was calculated according to the total proportion of Q2+Q3 quadrants. In order to determine the protective effects of the proteins against apoptosis of H_2O_2 oxidatively damaged cells, the apoptosis rate of different groups was detected by flow cytometry

(Fig. 5). The apoptosis rate (Q2+Q3) of the negative control group cells (untreated group) was 1.32% ± 0.21% (Fig. 5A), while the positive control group (1400 μmol/L H_2O_2) was 38.80 ± 2.12% (Fig. 5B). The apoptosis rate of cells pretreated with four proteins (TAT-*Sh*MT, TAT-*Sh*MT1, TAT-*Sh*MT2, and TAT-*Sh*MT3) decreased to 32.53% ± 1.33%, 24.36% ± 1.25%, 18.90% ± 2.12% and 14.06% ±1.27%, respectively (Fig. 5C, D, E, F). The results showed that H_2O_2 could lead to the occurrence of apoptosis, but protein-pretreatment reduced the apoptosis rate, and the apoptosis rate of cells treated with TAT-*Sh*MT3 was significantly lower than that of the control group, reaching a very significant level ($p < 0.01$).

The above results indicate that TAT-*Sh*MT3 pretreatment could significantly reduce the level of cellular oxidative stress, so the following experiments further validate using TAT-*Sh*MT3 as a repair substance.

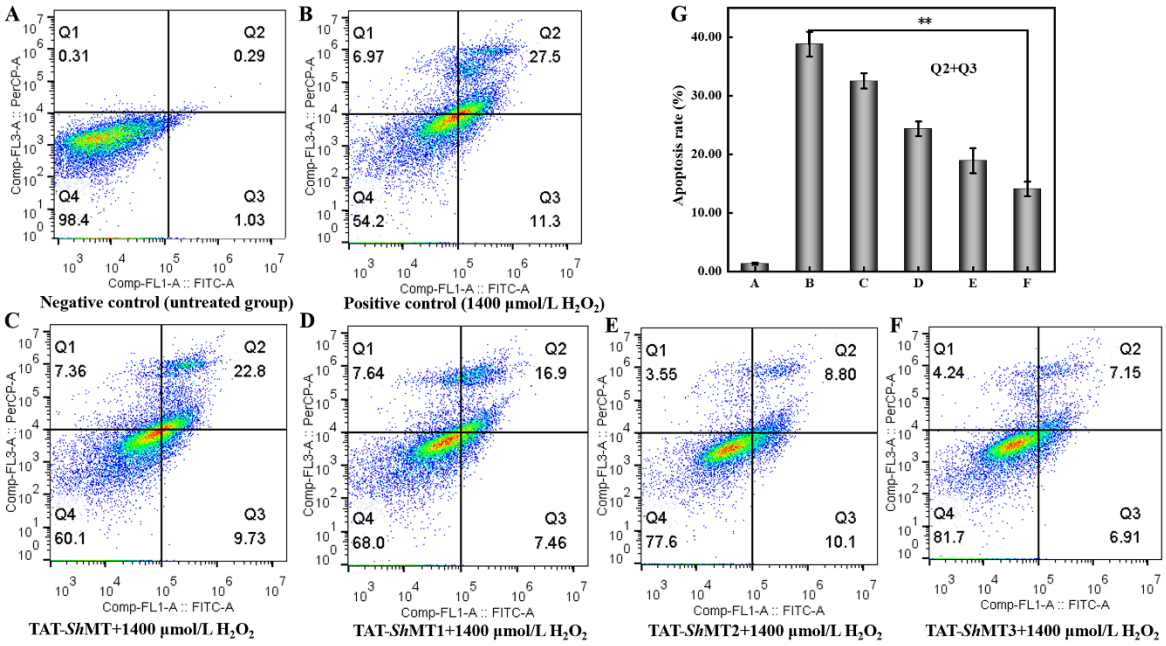

Fig. 5. Determination of apoptosis in different treatment groups. (A) Negative Contral (untreated group); (B) Positive control group (1400 μmol/L H_2O_2); (C) TAT-*Sh*MT+1400 μmol/L H_2O_2; (D) TAT-*Sh*MT1+1400 μmol/L H_2O_2; (E) TAT-*Sh*MT2+1400 μmol/L H_2O_2; (F)

TAT-*Sh*MT3+1400 μmol/L H_2O_2; (G) Apoptosis in different treatment groups.

3.6 ROS determination and Caspase-3 and Caspase-9 activities in different groups

The increase of ROS levels in cells represents an increase in the degree of oxidative damage. The results of ROS assay showed significantly increased fluorescence intensity in the positive control group (1400 μmol/L H_2O_2) compared to the negative control group (blank control), indicating a significant increase in intracellular ROS levels that put the cells in a state of oxidative stress. However, compared with the positive control group, the ROS level in the repair group significantly decreased, indicating that TAT-*Sh*MT3 pretreatment could reduce the ROS level in cells, thereby reducing the degree of oxidative stress in cells (Fig. 6A).

To investigate whether the antioxidant activity of proteins in H_2O_2-induced 293T cells were related to the apoptosis-related proteins Caspase-3 and Caspase-9 [52], the activities of Caspase-3 and Caspase-9 at the mRNA level and protein level were analyzed, respectively. The mRNA expression of Caspase-9 and Caspase-3 in H_2O_2 treated cells was significantly higher than that in the control group. However, co-treatment with TAT-*Sh*MT3 inhibited mRNA expression (Fig. 6C, D). These results indicate that TAT-*Sh*MT3 reduces H_2O_2 induced cell apoptosis by reducing the expression of Caspase-9 and Caspase-3. Similarly, TAT-*Sh*MT3 pretreatment significantly reduced the activity of Caspase-3 and Caspase-9 in cells ($P<0.05$) (Fig. 6B). This result suggests that TAT-*Sh*MT3 reduces Caspase-3 and Caspase-9 activity by inhibiting H_2O_2-induced oxidative damage in 293T cells, co-decreasing the rate of apoptosis [53].

Journal Pre-proof

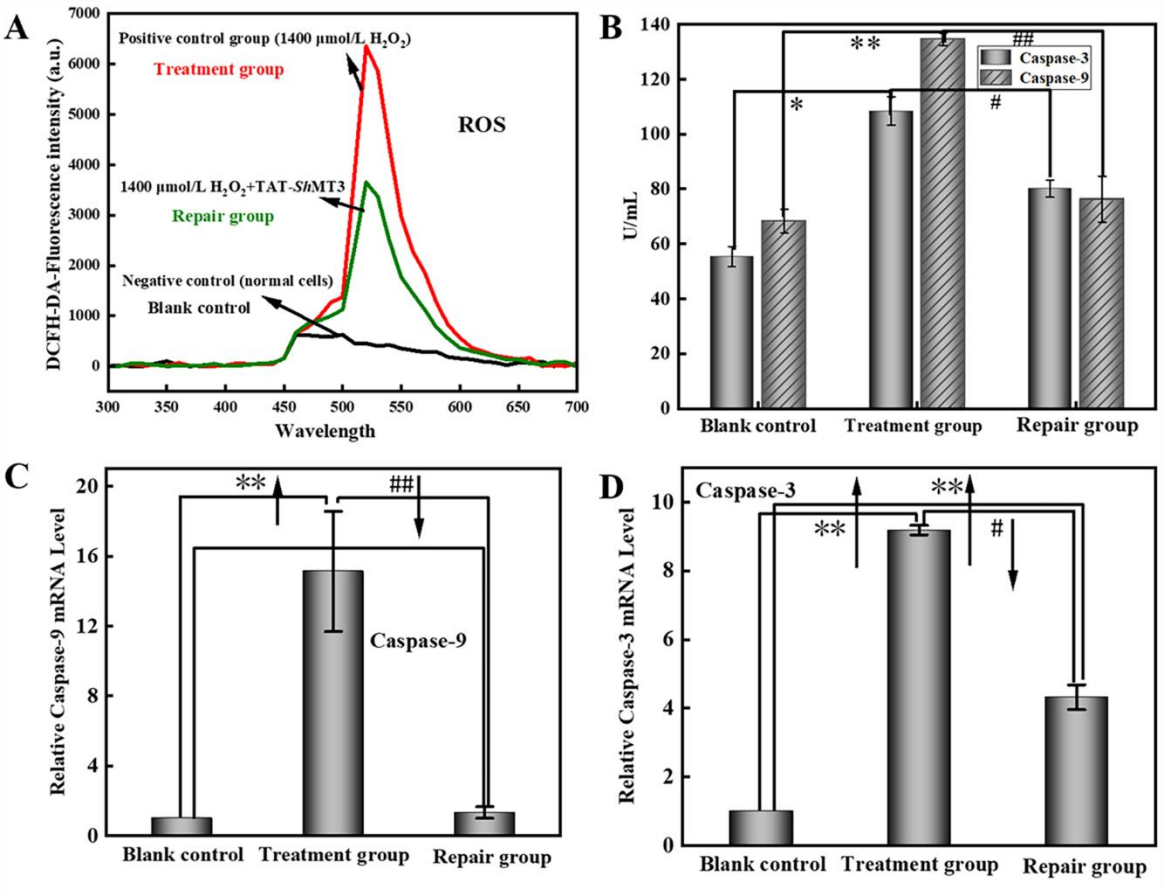

Fig. 6. ROS level, the mRNA expression and protein activity of Caspase-3 and Caspase-9 in different groups. (A) ROS level measurement. (B) Analysis of Caspase-3 and Caspase-9 protein activity; (C) Real-time qPCR analysis of Caspase-9 gene expression; (D) Real-time qPCR analysis of Caspase-3 gene expression.

3.7 Construction of GFP fusion vector by SOE-PCR

Although the modified protein TAT-*Sh*MT3 with increased antioxidant capacity was screened, its practical application was limited due to its poor stability and easy degradation. Therefore, we prepared a protein containing material through immobilization to improve its stability [54]. In order to facilitate the observation of the material's transmembrane ability, the GFP fluorescent tag was introduced by SOE-PCR [55-56]. The results showed that in the first

step of PCR, a 245 bp *TAT-ShMT3*-overlapping fragment containing a back-end overlapping fragment was obtained (Fig. 7A (Lane 1, Lane 2)). Similarly, in the second step of PCR, a 740 bp *GFP*- overlapping fragment containing a front -end overlap fragment was obtained (Fig. 7A (Lane 3, Lane 4, Lane 5, Lane 6)). Next, the successfully sequenced overlap fragment obtained in the first two steps was used as a double template for the third PCR step, and the overlap fragment was ligated to the pMD-19T vector for sequencing, which showed that a 946 bp successfully sequenced overlap fragment *TAT-ShMT3-GFP* was obtained (Fig. 7B (Lane 1)). Finally, B*am*H I and X*ho*l I nucleic acid endonuclease were used to double digest the expression vector pET28a- (Fig. 7C (Lane 1, Lane 2)) and the target fragment pMD-19T-TAT-*Sh*MT3-GFP (Fig. 1C7(Lane 3)), and the obtained digested fragments were recycled and linked with T4-DNA Ligase to construct the expression vector. The sequencing results showed that the expression vector pET28a-TAT-*Sh*MT3-GFP was successfully constructed (Fig. S5). The complete pattern diagram of vector construction is shown in Fig. 7D.

Journal Pre-proof

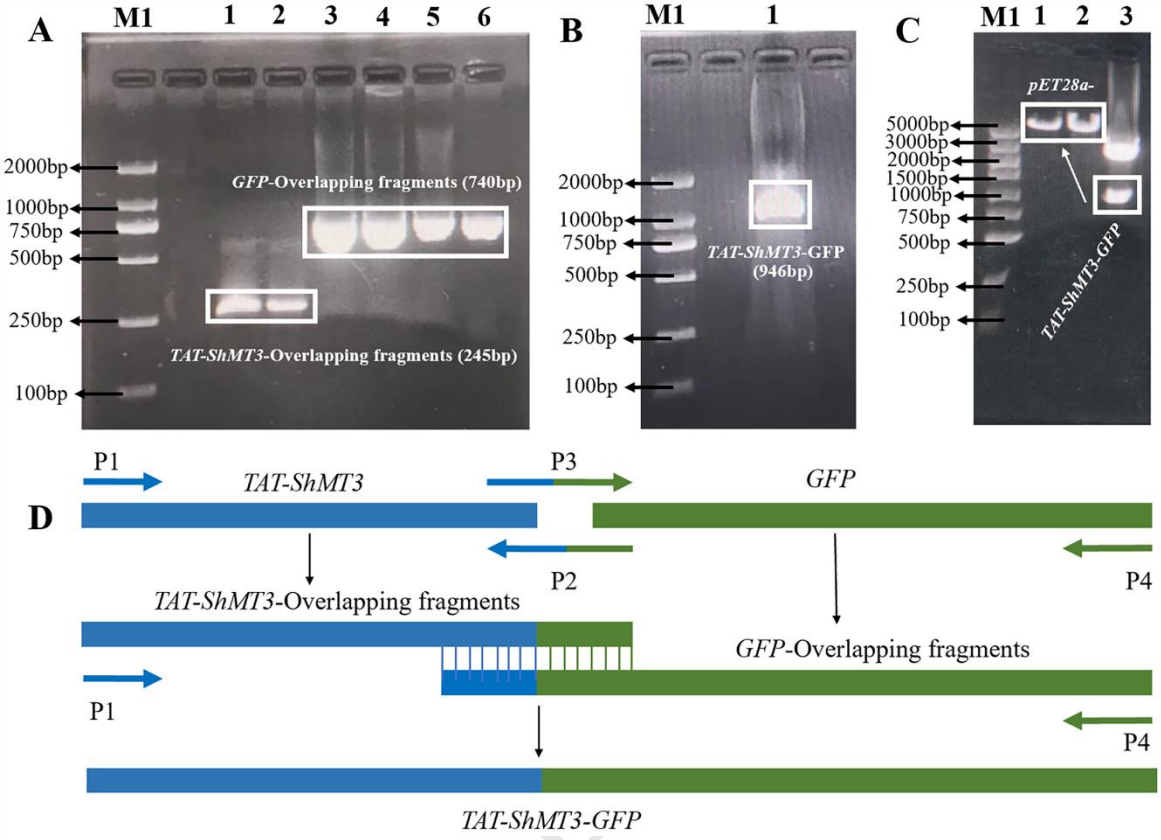

Fig. 7. SOE-PCR strategy for integrating the GFP fusion vector. (A) Generate single fragments through the first two steps of PCR. M1: Nucleic acid marker; Lane 1, 2: *TAT-ShMT3*-Overlapping, Lane 3-6: *GFP*-Overlapping; (B) Step 3 PCR to generate overlapping fragments *TAT-ShMT3-GFP*; (C) Double digestion of expression vector and target fragment; (D) Complete pattern diagram of vector construction.

3.8 Protein expression and validation of its binding with AuNPs

The successfully sequenced expression vector pET28a-TAT-*Sh*MT3-GFP was transformed into *E. coli*-BL21 (DE3) competent cells for induced expression of the target protein. The results showed that a large amount of soluble protein was obtained by adding 1mM IPTG at 37 ℃ for 7 h (180 rpm) (Fig. 8A1 (Lane 2)). The results also showed that the protein could not be expressed without IPTG induction (Fig. 8A1 (Lane 1)). Therefore, IPTG induction is a necessary condition

for protein prokaryotic expression [30].

Besides, we performed Western Blot experiments to verify the results of protein expression using Mouse anti His-Tag mAb as primary antibody and Goat Anti Mouse IgG H&L as secondary antibody. The results showed that TAT-*Sh*MT3-GFP appeared at 37 KDa, consistent with the expected molecular weight (Fig. 8A3).

To initially verify the specific binding of TAT-*Sh*MT3-GFP and AuNPs, the crude protein was added to AuNPs solution to a final concentration of 20 μg/mL, and binding was performed at 4℃ [57]. After co-incubation for 12 h, the conjugate was centrifuged at 8000g for 5 min and the supernatant was taken for SDS-PAGE validation, the results showed that compared to the original protein solution, the content of TAT-*Sh*MT3-GFP in the supernatant was significantly reduced, while other miscellaneous proteins remained almost unchanged (Fig. 8A1 (Lane 3)), which indicates that TAT-*Sh*MT3-GFP and AuNPs can specifically bind. Further extending the incubation time to 24 h, it was found that TAT-*Sh*MT3-GFP in the supernatant almost completely disappeared (Fig. 8A1 (Lane 4)). This series of results demonstrated the binding of TAT-*Sh*MT3-GFP and AuNPs. The experimental process diagram of protein expression, purification, and TAT-*Sh*MT3-GFP binding with AuNPs was shown in Fig. S6. Through quantitative verification, the results showed that TAT-*Sh*MT3-GFP and AuNPs could almost completely bind when the ratio was 1:128 (quality ratio), and composite materials were prepared according to this ratio in subsequent experiments (Fig. S7).

In order to prepare in large quantities TAT-*Sh*MT3-GFP+AuNPs for subsequent experiments, TAT-*Sh*MT3-GFP was purified using nickel column chromatography [33]. The results showed that most of other miscellaneous proteins were removed by purification (Fig. 8A2).

Metallothionein is a multifunctional small molecule protein [58-59]. In addition to heavy

Journal Pre-proof

metal binding and antioxidant functions, it has been reported in the literatures that metallothionein also has antibacterial functions [60]. Therefore, we further verified the binding of TAT-*Sh*MT3-GFP and AuNPs by antibacterial experiment. In the growth curve experiment, it can be seen that the addition of TAT-*Sh*MT3-GFP significantly inhibited the growth of *E. coli* compared with the blank control group, while the inhibition effect of the AuNPs group alone was not significant, while the binding product group (TAT-*Sh*MT3-GFP+ AuNPs) regained a significant level of inhibition. This result further indicated the binding of TAT-*Sh*MT3-GFP and AuNPs (Fig. 8B1). Similarly, in the plate experiment, it was shown that compared with the blank control group and BSA group, the TAT-*Sh*MT3-GFP group had a significant antibacterial effect, while the AuNPs group had no significant antibacterial effect, but the TAT-*Sh*MT3-GFP+AuNPs group regained its antibacterial effect (Fig. 8B2). This result also indirectly proves the successful binding of AuNPs and TAT-*Sh*MT3-GFP.

Journal Pre-proof

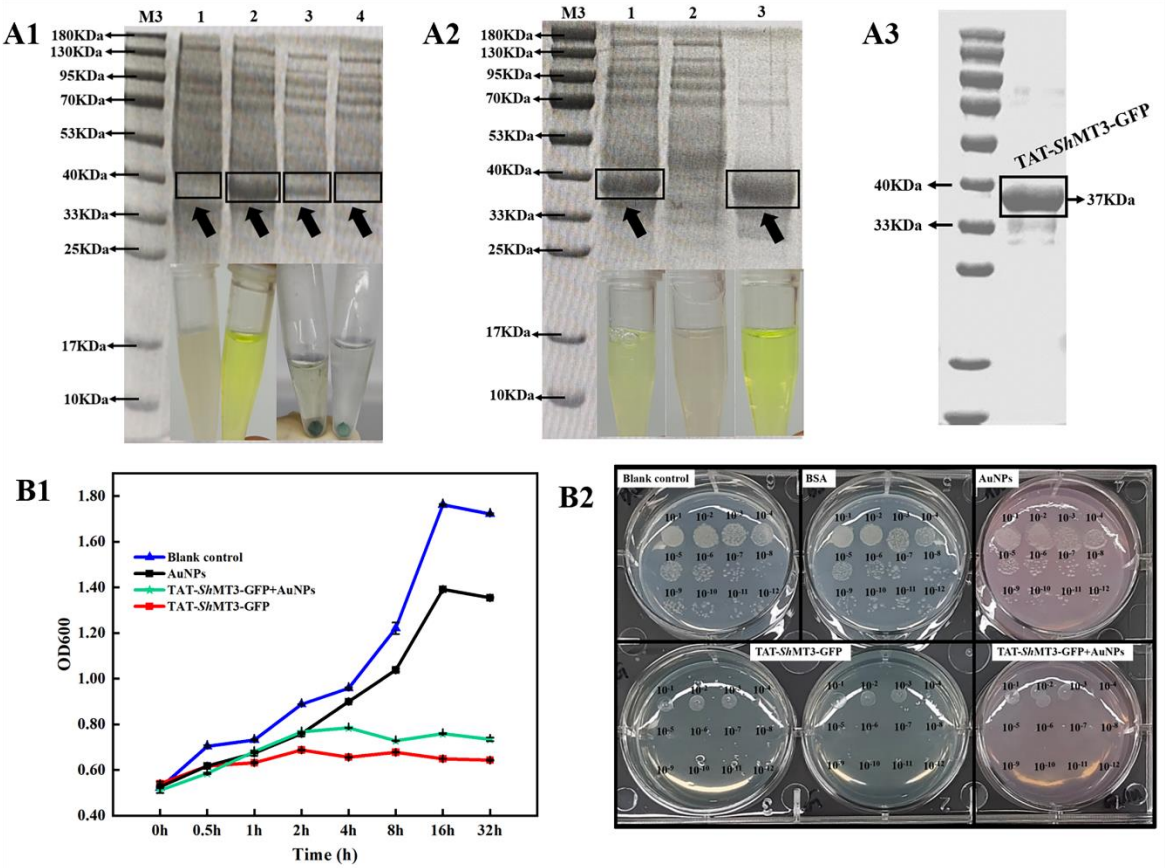

Fig. 8. Protein expression and validation of its binding with AuNPs. (A1) SDS-PAGE analysis of recombinant fusion proteins TAT-*Sh*MT3-GFP expression. M3: Protein marker; Lane 1: Uninduced; Lane 2: Induced; (A2) SDS-PAGE analysis of recombinant fusion proteins TAT-*Sh*MT3-GFP purification. Lane 1: Cell extract supernatants; Lane 2: Protein penetration; Lane 3: Protein purification solutions; (A3) Verification of TAT-*Sh*MT3-GFP expression by Western blot assay; (B1) *E. coli* growth curve validation the binding of TAT-*Sh*MT3-GFP and AuNPs; (B2) *E. coli* plate experiment validation the binding of TAT-*Sh*MT3-GFP and AuNPs.

The morphological and structural changes of TAT-*Sh*MT3-GFP combined with AuNPs are shown in Fig. 9. The results show that the particle size of single AuNP is 20 nm (Fig. 9A1, B1) and TAT-*Sh*MT3-GFP is 50-100 nm (Fig. 9B2). After binding with AuNPs, the surface of protein

becomes rougher (Fig. 9A2, A3). At the same time, TEM image shows “Island” structures, which is different from a dispersed state for TAT-*Sh*MT3-GFP (Fig. 9B2, B3). This may be due to the fact that AuNPs is bound to the surface of TAT-*Sh*MT3-GFP, making it easier to aggregate with each other.

Although the above results imply binding between AuNPs and TAT-*Sh*MT3-GFP, direct evidence is lacking. XPS is commonly used to characterize the binding of sulfhydryl groups and AuNPs. Therefore, XPS was used to directly demonstrate the binding of TAT-*Sh*MT3-GFP and AuNPs as well as to analyze the binding mechanism. XPS results showed that in the Au spectrum, AuNPs showed the results of Au4f, with peaks of Au4f $_{5/2}$ (83.8 eV) and Au4f $_{7/2}$ (87.5 eV), respectively. However, TAT-*Sh*MT3-GFP did not show any peaks, but after combining with AuNPs, Au4f $_{5/2}$ and Au4f $_{7/2}$ peaks reappeared (Fig. 9C1). In the S2p spectrum, since TAT-*Sh*MT3-GFP contains a large amount of Cys- and has R-SH bond, there is a strong peak at 164 eV in the S2p spectrum of TAT-*Sh*MT3-GFP, which indicates the existence of the -SH bond [62]. However, in the S2p spectrum of TAT-*Sh*MT3-GFP+AuNPs, we find that the peak has shifted, after binding, there is a -SH peak at 164 eV and an Au-S peak at 162.5 eV in this spectrum (Fig. 9C2). This result indicates that AuNPs covalently binds to TAT-*Sh*MT3-GFP through Au-S [63]. The FT-IR spectroscopy results show that the strength of the amide band and the strength of the -S-H peak also decreased after the combination of TAT-*Sh*MT3-GFP and AuNPs, which may be because the formation of Au-S bond consumes -S-H. This result also indicates the covalent bonding of TAT-*Sh*MT3-GFP and AuNPs (Fig. S8).

Based on the above conclusions, we concluded that AuNPs and TAT-*Sh*MT3-GFP were successfully bound with Au-S bonds.

Journal Pre-proof

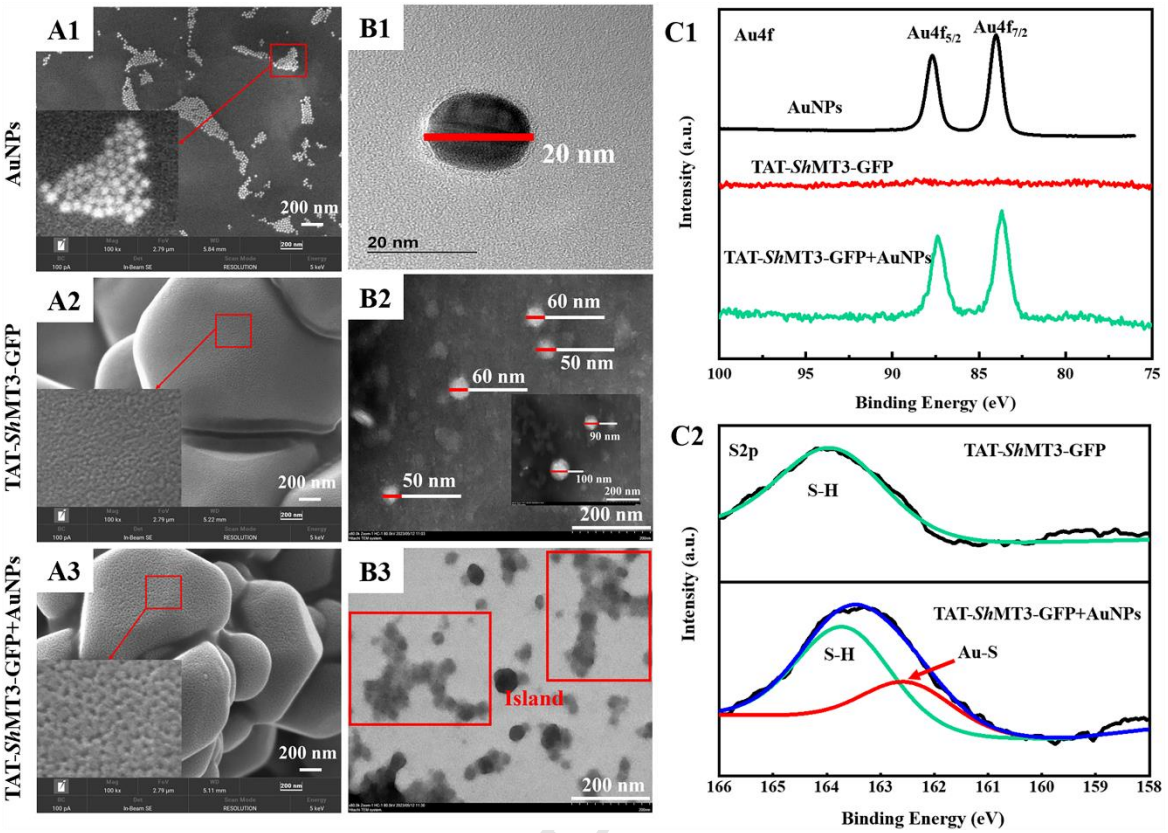

Fig. 9. Validation of the binding mechanism of TAT-*Sh*MT3-GFP and AuNPs. (A) The SEM results of AuNPs (A1), TAT-*Sh*MT3-GFP (A2) and TAT-*Sh*MT3-GFP+AuNPs (A3). (B) The TEM results of AuNPs (B1), TAT-*Sh*MT3-GFP (B2) and TAT-*Sh*MT3-GFP+AuNPs (B3). (C) The XPS results of Au4f (C1) and S2p (C2).

3.9 Transmembrane validation

In order to verify whether the binding of AuNPs with TAT-*Sh*MT3-GFP affected its transmembrane ability, fluorescence microscope was performed on cells of different treatment groups. The results showed that no green fluorescence was observed in the blank control group and the alone AuNPs group (Fig. 10A, B). Both TAT-*Sh*MT3-GFP and TAT-*Sh*MT3-GFP+AuNPs groups showed green fluorescence (Fig. 10C, D), indicating that they can efficiently penetrate the cell membrane and enter the cells.

Collect two groups of cells treated with TAT-*Sh*MT3-GFP and TAT-*Sh*MT3-GFP+AuNPs to measure their fluorescence values. The normalization calculation results showed that the relative fluorescence intensity only decreased from 1.08 to 1.00 after binding with AuNPs, but did not reach a significant level ($P > 0.05$) (Fig. 10E). This result indicates that the introduction of AuNPs hardly affects the transmembrane ability of TAT-*Sh*MT3-GFP.

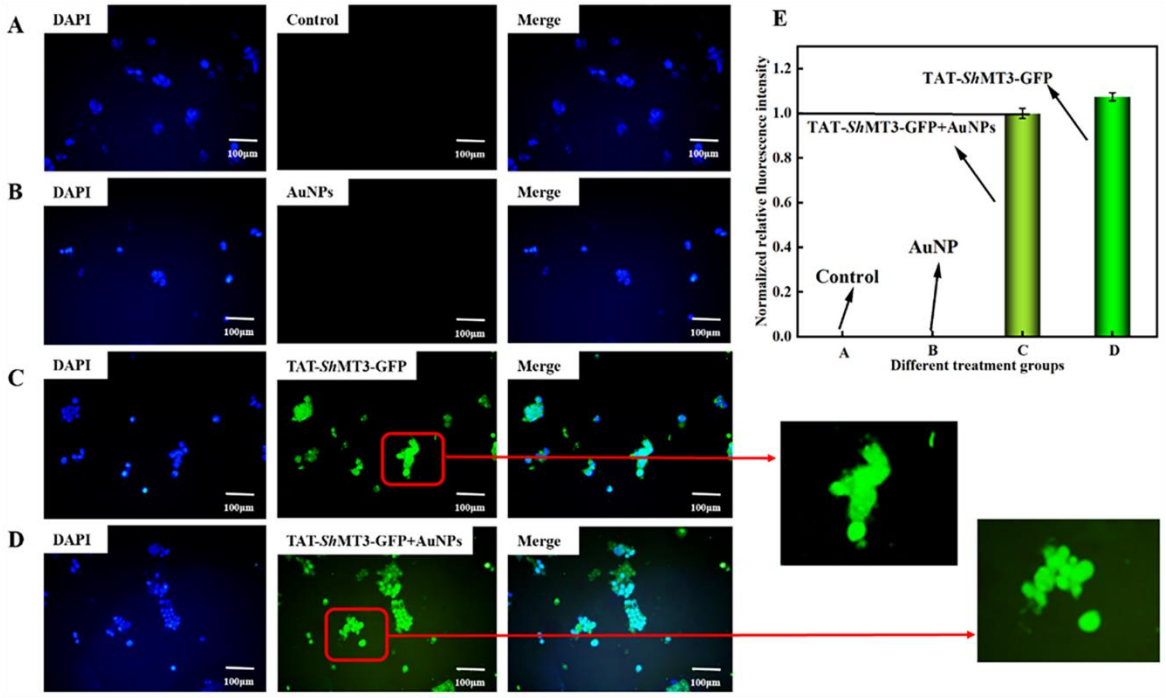

Fig. 10. Validation of transmembrane activity of cells in different treatment groups. (A) Blank control group; (B) AuNPs treatment group; (C) TAT-*Sh*MT3-GFP treatment group; (D) TAT-*Sh*MT3-GFP+AuNPs treatment group; (E) Determination of fluorescence values by Microplate Reader.

LDH (lactate dehydrogenase) is a stabilizing enzyme found in all cells and is rapidly released into the cell culture medium when the cell membrane is disrupted [64]. Therefore, the amount of LDH in the cell culture medium can be used to measure the integrity of the cell

membrane. The results showed that in cell lysate, the relative content of LDH in the cell culture medium was as high as 90.99% ± 0.41% because the cells were completely disrupted, while the relative content of LDH in the cell culture medium of normal cells was only 5.23% ± 0.02% because of the relative integrity of the cell membrane. After treatment with TAT-*Sh*MT3-GFP+AuNPs for 0.5 h, 1 h, 2 h and 4 h respectively, the relative content of LDH in the cell culture medium was still very little, indicating that TAT-*Sh*MT3-GFP+AuNPs did not damage the cells (Fig. 11A).

The results of transmembrane experiment showed that TAT-*Sh*MT3-GFP+AuNPs had completely diffused in the cytoplasm after 2 h of incubation (Fig. 11B). Therefore, based on this result, we speculate that TAT-*Sh*MT3-GFP+AuNPs can play a role in all organelles.

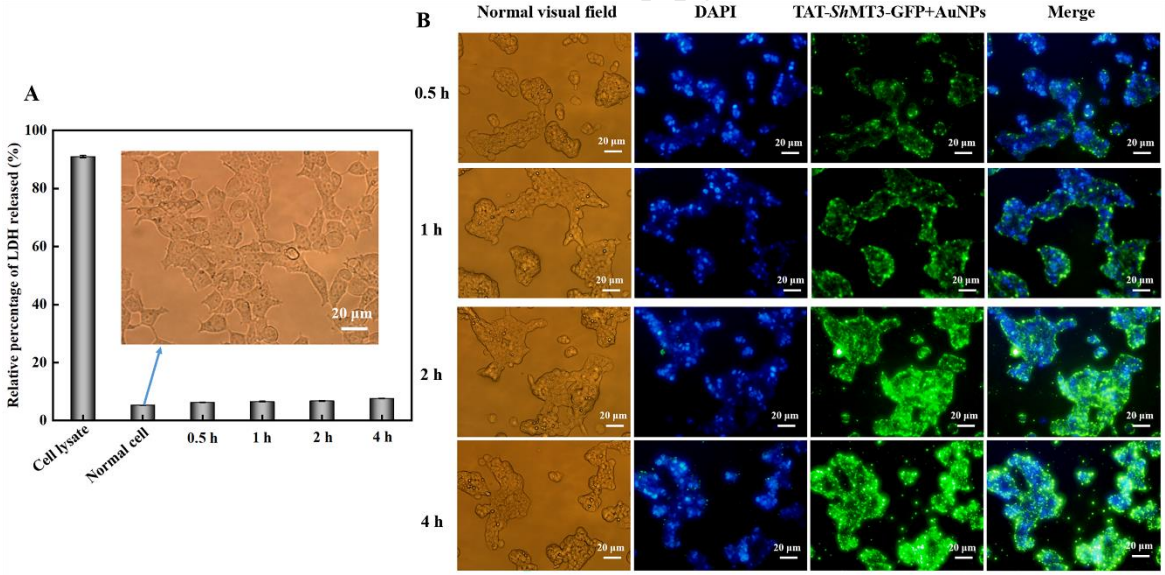

Fig. 11. (A) Relative activity of lactate dehydrogenase (LDH) in cell culture media of different treatment groups. (B) Transmembrane effect of TAT-*Sh*MT3-GFP+AuNPs at different times.

3.10 Cytotoxicity and ROS determination

To determine the cytotoxicity of recombinant fusion protein TAT-*Sh*MT3-GFP and

TAT-*Sh*MT3-GFP+AuNPs at different concentrations, the cck8 experiment was used for validation [65]. The results showed that when the protein concentration reached 400 μg/mL, it was almost non-toxic to cells, and when the protein concentration reached 800 μg/mL, the cell survival rate slightly decreased, but did not reach a significant level. 20 μg/mL-AuNPs was almost non-toxic to cells, consistent with literature reports [57]. When different concentrations of the protein were covalently bound to 20 μg/mL-AuNPs, the obtained material was also almost non-cytotoxic over a range of concentrations (Fig. 12A). These results suggest that TAT-*Sh*MT3-GFP+AuNPs can be used as a potential biosafe intracellular functional material.

As a product of oxidative stress, ROS can measure the degree of oxidative stress in cells, and the DCFH-DA probe assay was used to determine the ROS levels in cells from different treatment groups [66].The results of the ROS assay showed a significant increase in fluorescence values of the positive control group treated with 1400 μmol/L H_2O_2 compared to the negative control group, indicating that the intracellular ROS levels were significantly increased, placing the cells in a state of oxidative stress. However, in the TAT-*Sh*MT3-GFP and TAT-*Sh*MT3-GFP+AuNPs pretreated cells groups, the fluorescence intensity values were significantly lower, indicating that the TAT-*Sh*MT3-GFP and TAT-*Sh*MT3-GFP+AuNPs treatment was able to reduce the level of ROS in the treated cells, thereby reducing the degree of oxidative stress in the cells (Fig. 12B). As can be seen from the results of Fig. 12B, the antioxidant capacity of TAT-*Sh*MT3-GFP and TAT-*Sh*MT3-GFP+AuNPs was almost the same, indicating that the introduction of AuNPs did not affect the antioxidant capacity of TAT-*Sh*MT3-GFP.

Journal Pre-proof

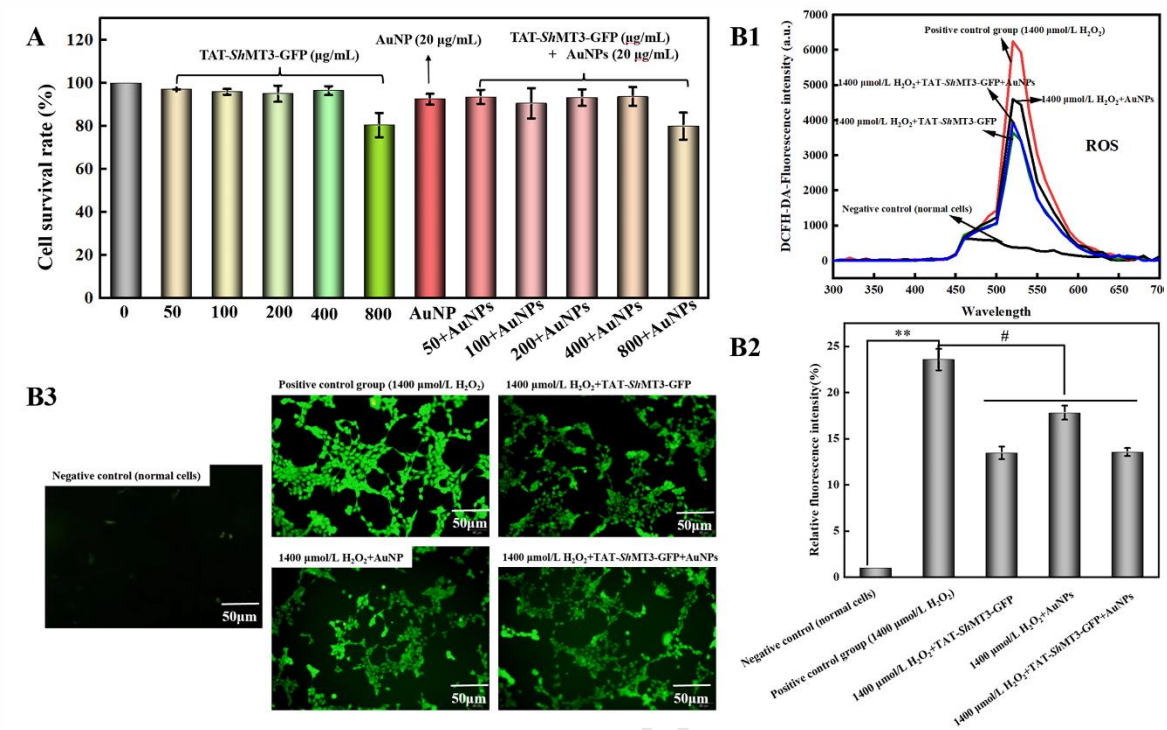

Fig. 12. Determination of cytotoxicity and ROS levels in 293T cells. (A) Cytotoxicity test of different concentrations TAT-*Sh*MT3-GFP and TAT-*Sh*MT3-GFP+AuNPs on 293T cell. (B) Determination of ROS levels in 293T cells; (B1) Measurement of fluorescence intensity values of different treatment groups; (B2) Calculation of relative fluorescence intensity of different treatment groups; (B3) Fluorescence imaging of different treatment groups observed by fluorescence microscopy (partial).

3.11 Stability analysis

This section investigated the influence of AuNPs on the stability of metallothionein from two aspects: thermal stability and degradation stability. Fig. 12A showed the thermogravimetric curves of AuNPs, metallothionein (TAT-*Sh*MT3-GFP), and TAT-*Sh*MT3-GFP+AuNPs complexes. The results showed that AuNPs hardly decomposed in a nitrogen atmosphere until 800°C. TGA curves of TAT-*Sh*MT3-GFP and TAT-*Sh*MT3-GFP+AuNPs showed a sharp thermal

decomposition at 170-250℃, which indicated that inorganic phosphate from PBS reagent decomposed and dehydrated to acid pyrophosphate [67-68]. In addition, the weight loss between 250 and 380℃ was attributed to the thermal decomposition of TAT-*Sh*MT3-GFP [69]. It could be seen that after combining with AuNPs, the thermal decomposition temperature of TAT-*Sh*MT3-GFP increased from 300℃ to 320℃, and the yield increased from~70% to~85% after 800℃. This demonstrated that the combination of AuNPs and TAT-*Sh*MT3-GFP could effectively increase the thermal stability of metallothionein under the combined action of a strong stable Au-S bond and the interaction between AuNPs with high thermal stability and metallothionein.

Analysis of the protein degradation rate in pure protein TAT-*Sh*MT3-GFP and binding material TAT-*Sh*MT3-GFP+AuNPs through BCA protein concentration measurement showed that the degradation of the proteins all went through three phases: stabilization phase, rapid degradation phase, and slow degradation phase. The retention rate of the proteins after the binding of TAT-*Sh*MT3-GFP with AuNPs was significantly higher than that of the proteins alone (Fig. 12B). This result suggests that the combination of TAT-*Sh*MT3-GFP with AuNPs could reduce the degradation rate of the protein and thus improve its degradation stability.

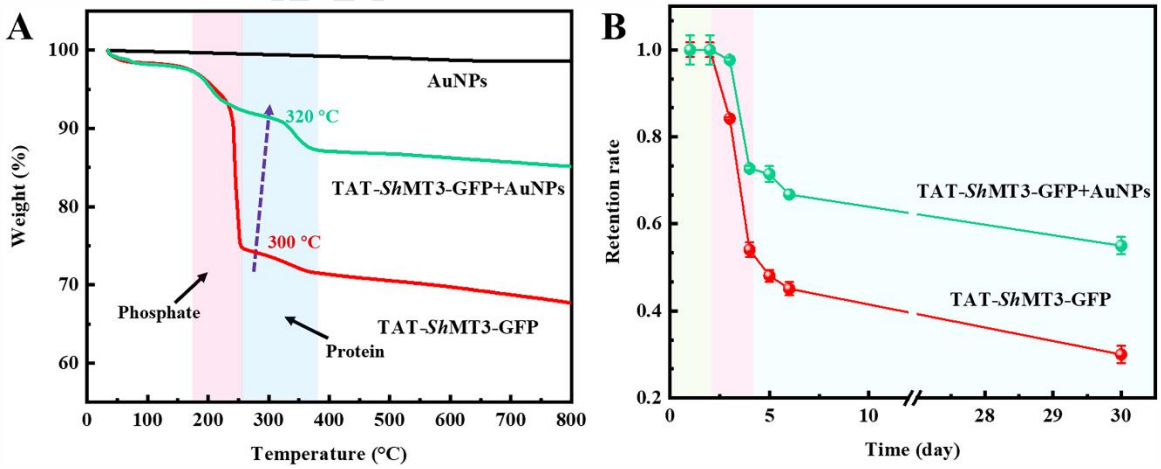

Fig. 13. Analysis of thermal stability and degradation stability. (A) TGA analysis of AuNPs,

TAT-*Sh*MT3-GFP and TAT-*Sh*MT3-GFP+AuNPs. (B) Degradation stability analysis of TAT-*Sh*MT3-GFP and TAT-*Sh*MT3-GFP+AuNPs.

4. Conclusion

This study first constructed four prokaryotic expression vectors that fused transmembrane penetrating peptide TAT, and induced the expression of modified proteins. The transmembrane activity of the four modified proteins was verified through immunofluorescence experiments, and the antioxidant activity of the four modified proteins was also verified. The modified protein TAT-*Sh*MT3 was screened to have the strongest antioxidant activity. To further simplify the imaging of proteins in cells, the *TAT-ShMT3* and *GFP* genes were fused by SOE-PCR, and the fusion protein TAT-*Sh*MT3-GFP was expressed in *E. coli*. In addition, TAT-*Sh*MT3-GFP was covalently combined with AuNPs through immobilization to obtain the immobilized material TAT-*Sh*MT3-GFP+AuNPs. The binding of TAT-*Sh*MT3-GFP with AuNPs was validated by antibacterial experiments, XPS, SEM and TEM, and the transmembrane activity, antioxidant activity and stability of TAT-*Sh*MT3-GFP+AuNPs were investigated. The results indicated that this study has prepared a novel material (TAT-*Sh*MT3-GFP+AuNPs) with high transmembrane ability, antioxidant activity, fluorescence visualization and stability was prepared, which providing new ideas for the further application of metallothionein.

Credit Author Statement

Xuefen Li: performed experiments, analyzed data, made graphics, and wrote the manuscript. **Hui Liu** and **Yuxia Wang:** Auxiliary experiment. **M. James C. Crabbe:** writing, review & editing. **Lan Wang:** Project administration. **Wenli Ma:** Supervision, Project

Journal Pre-proof

administration, Funding acquisition, review & editing. **Zhumei Ren:** review & editing.

Declaration of Competing Interest

The authors declare that they have no known competing financial interests or personal relationships that could have appeared to influence the work reported in this paper.

Acknowledgement

This work was supported by the National Natural Science Foundation of China (31672293) and Natural Science Foundation of Shanxi Province (4049920).

References

[1] D.H. Hamer, METALLOTHIONEIN, Ann. Rev. Biochem. 55 (1986) 913-951. https://doi.org/10.1146/annurev.biochem.55.1.913.

[2] C. Cobbett, P. Goldsbrough, Phytochelatins and metallothioneins: roles in heavy metal detoxification and homeostasis, Annu. Rev. Plant Biol. 53 (2002) 159-82. https://doi.org/10.1146/annurev.arplant.53.100301.135154.

[3] H.Z. Yang, W.J. Gu, W. Chen, J.S. Hwang, L. Wang, Metal binding characterization of heterologously expressed metallothionein of the freshwater crab Sinopotamon henanense, Chemosphere. 235 (2019) 926-934. https://doi.org/10.1016/j.chemosphere.2019.06.097.

[4] P.J. Thornalley, M. Vasak, Possible role for metallothionein in protection against radiation-induced oxidative stress. Kinetics and mechanism of its reaction with superoxide and hydroxyl radicals, BBA. 827 (1985) 36-44. https://doi.org/10.1016/0167-4838(85)90098-6.

[5] M. SATO, I. BREMNER, OXYGEN FREE RADICALS AND METALLOTHIONEIN, Free Radical Bio. Med. 14 (1993) 325-337. https://doi.org/10.1016/0891-5849(93)90029-T.

[6] M.S. Samuel, S. Datta, R.S. Khandge, E. Selvarajan, A state of the art review on

Journal Pre-proof

characterization of heavy metal binding metallothioneins proteins and their widespread applications, Sci. Total Eeviron. 775 (2021). https://doi.org/10.1016/j.scitotenv.2021.145829.

[7] M. Si, J. Lang, The roles of metallothioneins in carcinogenesis, J. Hematol. Oncol. 11 (2018) 107. https://doi.org/10.1186/s13045-018-0645-x.

[8] Y. PARK, J. Zhang, L. CAI, Reappraisal of metallothionein: Clinical implications for patients with diabetes mellitus, J. Diabetes. 3 (2018) 213-231. https://doi.org/10.1111/jdb.12620.

[9] Q. Zhou, D. Yang, M. Wu, Y. Guo, W. Guo, L. Zhong, X. Cai, A. Dai, W. Jang, E.I. Shakhnovich, Z.J. Liu, R.C. Stevens, N.A. Lambert, M.M. Babu, M.W. Wang, S. Zhao, Common activation mechanism of class A GPCRs, Elife. 8 (2019). https://doi.org/10.7554/eLife.50279.

[10] C.S. Silva, A. Nayak, X. Lai, S. Hutin, V. Hugouvieux, J.H. Jung, I. Lopez-Vidriero, J.M. Franco-Zorrilla, K.C.S. Panigrahi, M.H. Nanao, P.A. Wigge, C. Zubieta, Molecular mechanisms of Evening Complex activity in Arabidopsis, PANS. 117 (2020) 6901-6909. https://doi.org/10.1073/pnas.1920972117.

[11] J. Zhao, Q. Wang, X. Ni, S. Shen, C. Nan, X. Li, X. Chen, F. Yang, Dissecting the essential role of N-glycosylation in catalytic performance of xanthan lyase, Bioresour. Bioprocess. 9 (2022). https://doi.org/10.1186/s40643-022-00620-5.

[12] X. Wang, Y. Nie, Y. Xu, Industrially produced pullulanases with thermostability: Discovery, engineering, and heterologous expression, Bioresour. Technol. 278 (2019) 360-371. https://doi.org/10.1016/j.biortech.2019.01.098.

[13] X. Li, Z. Ren, M.J.C. Crabbe, L. Wang, W. Ma, Genetic modifications of metallothionein enhance the tolerance and bioaccumulation of heavy metals in Escherichia coli, Ecotoxicol.

Environ. Saf. 222 (2021) 112512. https://doi.org/10.1016/j.ecoenv.2021.112512.

[14] X. Li, Y. Wang, M.J.C. Crabbe, L. Wang, W. Ma, Z. Ren, Genetically modified metallothionein/cellulose composite material as an efficient and environmentally friendly biosorbent for Cd^{2+} removal, Int. J. Biol. Macromol. 218 (2022) 543-555. https://doi.org/10.1016/j.ijbiomac.2022.07.144.

[15] Y. He, W. Ma, Y. Li, J. Liu, W. Jing, L. Wang, Expression of metallothionein of freshwater crab (Sinopotamon henanense) in Escherichia coli enhances tolerance and accumulation of zinc, copper and cadmium, Ecotoxicology 23 (2014) 56-64. https://doi.org/10.1007/s10646-013-1151-0.

[16] A.I. Freitas, L. Domingues, T.Q. Aguiar, Tag-mediated single-step purification and immobilization of recombinant proteins toward protein-engineered advanced materials, J. Adv. Res. 36 (2022) 249-264. https://doi.org/10.1016/j.jare.2021.06.010.

[17] Z. Ashkan, R. Hemmati, A. Homaei, A. Dinari, M. Jamlidoost, A. Tashakor, Immobilization of enzymes on nanoinorganic support materials: An update, Int. J. Biol. Macromol. 168 (2021) 708-721. https://doi.org/10.1016/j.ijbiomac.2020.11.127.

[18] L. Vigderman, E.R. Zubarev, Therapeutic platforms based on gold nanoparticles and their covalent conjugates with drug molecules, Adv. Drug Deliv. Rev. 65 (2013) 663-76. https://doi.org/10.1016/j.addr.2012.05.004.

[19] J. Zhang, L. Mou, X. Jiang, Surface chemistry of gold nanoparticles for health-related applications, Chem. Sci. 11 (2020) 923-936. https://doi.org/10.1039/c9sc06497d.

[20] A.J. Mieszawska, W.J. Mulder, Z.A. Fayad, D.P. Cormode, Multifunctional gold nanoparticles for diagnosis and therapy of disease, Mol. Pharm. 10 (2013) 831-47. https://doi.org/10.1021/mp3005885.

Journal Pre-proof

[21] P. Singh, S. Pandit, V. Mokkapati, A. Garg, V. Ravikumar, I. Mijakovic, Gold Nanoparticles in Diagnostics and Therapeutics for Human Cancer, Int. J. Mol. Sci. 19 (2018). https://doi.org/10.3390/ijms19071979.

[22] Y. Ding, Z. Jiang, K. Saha, C.S. Kim, S.T. Kim, R.F. Landis, V.M. Rotello, Gold nanoparticles for nucleic acid delivery, Mol. Ther. 22 (2014) 1075-1083. https://doi.org/10.1038/mt.2014.30.

[23] Y.C. Yeh, B. Creran, V.M. Rotello, Gold nanoparticles: preparation, properties, and applications in bionanotechnology, Nanoscale 4 (2012) 1871-80. https://doi.org/10.1039/c1nr11188d.

[24] M. Capdevila, R. Bofill, Ò. Palacios, S. Atrian, State-of-the-art of metallothioneins at the beginning of the 21st century, Coord. Chem. Rev. 256 (2012) 46-62. https://doi.org/10.1016/j.ccr.2011.07.006.

[25] Y. Zhang, J. Hao, X. Xu, X. Chen, J. Wang, Protein Corona-Triggered Catalytic Inhibition of Insufficient POSS Polymer-Caged Gold Nanoparticles for Sensitive Colorimetric Detection of Metallothioneins, Anal. Chem. 92 (2020) 2080-2087. https://doi.org/10.1021/acs.analchem.9b04593.

[26] N. Kim, S.H. Son, Development of Antigen-Immobilized Metallothionein Sensor that Exploits Gold Nanoparticle-Based Enhancement of Signal, J. Nanosci. Nanotechnol. 15 (2015) 6188-92. https://doi.org/10.1166/jnn.2015.10297.

[27] S.A. Ditta, A. Yaqub, F. Tanvir, M. Rashid, R. Ullah, M. Zubair, S. Ali, K.M. Anjum, Gold nanoparticles capped with L-glycine, L-cystine, and L-tyrosine: toxicity profiling and antioxidant potential, J. Mater. Sci. 58 (2023) 2814-2837. https://doi.org/10.1007/s10853-023-08209-9.

Journal Pre-proof

[28] L. Pan, Q. He, J. Liu, Y. Chen, M. Ma, L. Zhang, J. Shi, Nuclear-targeted drug delivery of TAT peptide-conjugated monodisperse mesoporous silica nanoparticles, J. Am. Chem. Soc. 134 (2012) 5722-5. https://doi.org/10.1021/ja211035w.

[29] K.S. Lim, M.H. Lim, Y.W. Won, J.K. Kim, Y.C. Kang, E.J. Park, J.W. Chae, S.M. Kim, S.E. Ryu, Y.K. Pak, Y.H. Kim, Dual-mode enhancement of metallothionein protein with cell transduction and retention peptide fusion, J. Control Release 171 (2013) 193-200. https://doi.org/10.1016/j.jconrel.2013.07.009.

[30] J.M. Xu, Z.S. Wu, K.J. Zhao, Z.J. Xi, L.Y. Wang, F. Cheng, Y.P. Xue, Y.G. Zheng, IPTG-induced high protein expression for whole-cell biosynthesis of L-phosphinothricin, Biotechnol. J. (2023) e2300027. https://doi.org/10.1002/biot.202300027.

[31] L. Gomes, G. Monteiro, F. Mergulhao, The Impact of IPTG Induction on Plasmid Stability and Heterologous Protein Expression by Escherichia coli Biofilms, Int. J. Mol. Sci. 21 (2020). https://doi.org/10.3390/ijms21020576.

[32] T.C. Yu, W.L. Liu, M.S. Brinck, J.E. Davis, J. Shek, G. Bower, T. Einav, K.D. Insigne, R. Phillips, S. Kosuri, G. Urtecho, Multiplexed characterization of rationally designed promoter architectures deconstructs combinatorial logic for IPTG-inducible systems, Nat. Commun. 12 (2021) 325. https://doi.org/10.1038/s41467-020-20094-3.

[33] H.E. Duran, S. Beydemir, Recombinant human carbonic anhydrase VII: Purification, characterization, inhibition, and molecular docking studies, Biotechnol Appl Biochem. 70 (2023) 415-428. https://doi.org/10.1002/bab.2367.

[34] J. Cheng, M. Ahmat, H. Guo, X. Wei, L. Zhang, Q. Cheng, J. Zhang, J. Wang, D. Si, Y. Zhang, R. Zhang, Expression, Purification and Characterization of a Novel Hybrid Peptide CLP with Excellent Antibacterial Activity, Molecules 26 (2021).

Journal Pre-proof

https://doi.org/10.3390/molecules26237142.

[35] C. Meng, K. Wang, X. Zhang, X. Zhu, Purification, secondary structure and antioxidant activity of metallothionein zinc-binding proteins from Arca subcrenata, Protein Expr. Purif. 182 (2021) 105838. https://doi.org/10.1016/j.pep.2021.105838.

[36] J. Kong, S. Yu, Fourier transform infrared spectroscopic analysis of protein secondary structures, Acta Biochim Biophys Sin (Shanghai) 39 (2007) 549-59. https://doi.org/10.1111/j.1745-7270.2007.00320.x.

[37] G.M. Mei, X.H. Wu, X.J. Zhang, J. Gu, Y. Fang, C.Y. Meng, W.G. Yang, Structural Characterization and In *Vitro* Antioxidant Activity of Metallothionein from Oratosquilla oratoria, Molecules 27 (2022). https://doi.org/10.3390/molecules27072320.

[38] R. Lu, W.W. Li, A. Katzir, Y. Raichlin, B. Mizaikoff, H.Q. Yu, Fourier transform infrared spectroscopy on external perturbations inducing secondary structure changes of hemoglobin, Analyst 141 (2016) 6061-6067. https://doi.org/10.1039/c6an01477a.

[39] C. Jung, Fourier transform infrared spectroscopy as a tool to study structural properties of cytochromes P450 (CYPs), Anal. Bioanal. Chem. 392 (2008) 1031-58. https://doi.org/10.1007/s00216-008-2216-4.

[40] E. Goormaghtigh, J.M. Ruysschaert, V. Raussens, Evaluation of the information content in infrared spectra for protein secondary structure determination, Biophys J. 90 (2006) 2946-57. https://doi.org/10.1529/biophysj.105.072017.

[41] S. Yang, Q. Zhang, H. Yang, H. Shi, A. Dong, L. Wang, S. Yu, Progress in infrared spectroscopy as an efficient tool for predicting protein secondary structure, Int. J. Biol. Macromol. 206 (2022) 175-187. https://doi.org/10.1016/j.ijbiomac.2022.02.104.

[42] A. Barth, Infrared spectroscopy of proteins, BBA 1767 (2007) 1073-101.

Journal Pre-proof

https://doi.org/10.1016/j.bbabio.2007.06.004.

[43] M.C. Manning, Use of infrared spectroscopy to monitor protein structure and stability, Expert Rev. Proteomics 2 (2005) 731-743. https://doi.org/10.1586/14789450.2.5.731.

[44] Z.S. Huang, Z.S. Wei, X.L. Xiao, B.L. Li, S. Ming, X.L. Cheng, H.Y. Jiao, Bioconversion of Hg^0 into HA-Hg for simultaneous removal of Hg^0 and NO in a denitrifying membrane biofilm reactor, Chemosphere 244 (2020) 125544. https://doi.org/10.1016/j.chemosphere.2019.125544.

[45] C. Meng, K. Wang, X. Zhang, X. Zhu, Purification and structure analysis of zinc-binding protein from Mizuhopecten yessoensis, J. Food Biochem. 45 (2021) e13756. https://doi.org/10.1111/jfbc.13756.

[46] G. Kan, Y. Ju, Y. Zhou, C. Shi, Y. Qiao, Y. Yang, R. Wang, X. Wang, Cloning and functional characterization of a novel metallothionein gene in Antarctic sea-ice yeast (Rhodotorula mucilaginosa), J. Basic Microbiol. 59 (2019) 879-889. https://doi.org/10.1002/jobm.201900240.

[47] J.R. Lin, B. Izar, S. Wang, C. Yapp, S. Mei, P.M. Shah, S. Santagata, P.K. Sorger, Highly multiplexed immunofluorescence imaging of human tissues and tumors using t-CyCIF and conventional optical microscopes, Elife 7 (2018). https://doi.org/10.7554/eLife.31657.

[48] S. Warinhomhoun, C. Muangnoi, V. Buranasudja, W. Mekboonsonglarp, P. Rojsitthisak, K. Likhitwitayawuid, B. Sritularak, Antioxidant Activities and Protective Effects of Dendropachol, a New Bisbibenzyl Compound from Dendrobium pachyglossum, on Hydrogen Peroxide-Induced Oxidative Stress in HaCaT Keratinocytes, Antioxidants (Basel) 10 (2021). https://doi.org/10.3390/antiox10020252.

[49] Y. Xiao, X. Zhang, Q. Huang, Protective effects of Cordyceps sinensis

Journal Pre-proof

exopolysaccharide-selenium nanoparticles on H(2)O(2)-induced oxidative stress in HepG2 cells, Int. J. Biol. Macromol. 213 (2022) 339-351. https://doi.org/10.1016/j.ijbiomac.2022.05.173.

[50] A. Adan, G. Alizada, Y. Kiraz, Y. Baran, A. Nalbant, Flow cytometry: basic principles and applications, Crit. Rev. Biotechnol. 37 (2017) 163-176. https://doi.org/10.3109/07388551.2015.1128876.

[51] J. Ren, L. Ding, D. Zhang, G. Shi, Q. Xu, S. Shen, Y. Wang, T. Wang, Y. Hou, Carcinoma-associated fibroblasts promote the stemness and chemoresistance of colorectal cancer by transferring exosomal lncRNA H19, Theranostics 8 (2018) 3932-3948. https://doi.org/10.7150/thno.25541.

[52] L.E. Araya, I.V. Soni, J.A. Hardy, O. Julien, Deorphanizing Caspase-3 and Caspase-9 Substrates In and Out of Apoptosis with Deep Substrate Profiling, ACS Chem. Biol. 16 (2021) 2280-2296. https://doi.org/10.1021/acschembio.1c00456.

[53] N. Xu, Y. Lu, J. Hou, C. Liu, Y. Sun, A Polysaccharide Purified from Morchella conica Pers. Prevents Oxidative Stress Induced by H(2)O(2) in Human Embryonic Kidney (HEK) 293T Cells, Int. J. Mol. Sci. 19 (2018). https://doi.org/10.3390/ijms19124027.

[54] C. Bernal, K. Rodriguez, R. Martinez, Integrating enzyme immobilization and protein engineering: An alternative path for the development of novel and improved industrial biocatalysts, Biotechnol. Adv. 36 (2018) 1470-1480. https://doi.org/10.1016/j.biotechadv.2018.06.002.

[55] J. Li, J. Ouyang, J. Yuan, T. Li, M. Luo, J. Wang, Y. Chen, Establishment and evaluation of an overlap extension polymerase chain reaction technique for rapid and efficient detection of drug-resistance in Mycobacterium tuberculosis, Infect. Dis. Poverty 11 (2022) 31.

Journal Pre-proof

https://doi.org/10.1186/s40249-022-00953-5.

[56] W. Ma, X. Li, Q. Wang, Z. Ren, M.J.C. Crabbe, L. Wang, Tandem oligomeric expression of metallothionein enhance heavy metal tolerance and bioaccumulation in Escherichia coli, Ecotoxicol. Environ. Saf. 181 (2019) 301-307. https://doi.org/10.1016/j.ecoenv.2019.06.022.

[57] M.V. Berberian, C.A. Pocognoni, L.S. Mayorga, A TEM-traceable physiologically functional gold nanoprobe that permeates non-endocytic cells, Int. J. Nanomedicine 13 (2018) 8075-8086. https://doi.org/10.2147/IJN.S168149.

[58] B. Ruttkay-Nedecky, L. Nejdl, J. Gumulec, O. Zitka, M. Masarik, T. Eckschlager, M. Stiborova, V. Adam, R. Kizek, The role of metallothionein in oxidative stress, Int. J. Mol. Sci. 14 (2013) 6044-66. https://doi.org/10.3390/ijms14036044.

[59] M. Nordberg, G.F. Nordberg, Metallothionein and Cadmium Toxicology-Historical Review and Commentary, Biomolecules 12 (2022). https://doi.org/10.3390/biom12030360.

[60] H.Y. JIN, Q. HUI, J.Y. JUN, A.C. JU, L.D. SEN, D.R. QIAN, Q.R. LIN, Preliminary Studies on the Zinc-Induced Metallothionein Protein with Antibacterial Activity in Housefly Larvae, Musca Domestica, ACTA Biol. Hhung. 56 (2005) 283–295. https://doi.org/10.1556/ABiol.56.2005.3-4.11.

[61] X. Song, C. Zhou, F. Fu, Z. Chen, Q. Wu, Effect of high-pressure homogenization on particle size and film properties of soy protein isolate, Ind. Crop. Prod. 43 (2013) 538-544. https://doi.org/10.1016/j.indcrop.2012.08.005.

[62] Z. Zhang, H. Karimi-Maleh, In situ synthesis of label-free electrochemical aptasensor-based sandwich-like AuNPss/PPy/Ti(3)C(2)T(x) for ultrasensitive detection of lead ions as hazardous pollutants in environmental fluids, Chemosphere 324 (2023) 138302.

Journal Pre-proof

https://doi.org/10.1016/j.chemosphere.2023.138302.

[63] A.Y. Polyakov, D.A. Kozlov, V.A. Lebedev, R.G. Chumakov, A.S. Frolov, L.V. Yashina, M.N. Rumyantseva, E.A. Goodilin, Gold Decoration and Photoresistive Response to Nitrogen Dioxide of WS(2) Nanotubes, Chemistry 24 (2018) 18952-18962. https://doi.org/10.1002/chem.201803502.

[64] N.K. Bari, S. Barua, A. Garg, M.K. Sannigrahi, S. Sinha, Cellulose-metallothionein matrix for metal binding, Carbohydr. Polym. 192 (2018), 126-134. https://doi.org/10.1016/j.carbpol.2018.03.043.

[65] N. Li, X. Xu, Y. Zhan, X. Fei, Y. Ouyang, P. Zheng, Y. Zhou, C. He, C. Xie, Y. Hu, J. Hong, N. Lu, Z. Ge, Y. Zhu, YAP and β-catenin cooperate to drive H. pylori-induced gastric tumorigenesis, Gut Microbes 15 (2023) 2192501. https://doi.org/10.1080/19490976.2023.2192501.

[66] B. Yang, Y. Chen, J. Shi, Reactive Oxygen Species (ROS)-Based Nanomedicine, Chem. Rev. 119 (2019) 4881-4985. https://doi.org/10.1021/acs.chemrev.8b00626.

[67] N. Jinlong, Z. Zhenxi, J. Dazong, Investigation of phase evolution during the formation of calcium potassium sodium orthophosphate, Mater. Chem. Phys. 78 (2002) 308–312. https://doi.org/10.1016/S0254-0584(02)00200-6.

[68] Y. Londo˜no, D. Pe˜na-Lara, J.u.E. Diosa, Comportamiento De Las Fases Del $NaH_2PO_4.H_2O$ a Altas Temperaturas Phase Behavior of $NaH_2PO_4.H_2O$ at High Temperatures, Momento 52 (2016) 1-8.

[69] Y. Xu, Y. Xu, Y. Han, M. Chen, W. Zhang, Q. Gao, J. Li, The Effect of Enzymolysis on Performance of Soy Protein-Based Adhesive, Molecules 23 (2018). https://doi.org/10.3390/molecules23112752.

Journal Pre-proof

Highlights

- TAT-*Sh*MT3 was obtained by long primer PCR.
- TAT-*Sh*MT3 has about 30% increase in antioxidant capacity compared to TAT-*Sh*MT.
- TAT-*Sh*MT3-GFP was obtained by SOE-PCR.
- TAT-*Sh*MT3-GFP+AuNPs was obtained Au-S covalent bond.
- TAT-ShMT3-GFP+AuNPs has higher stability compared to TAT-*Sh*MT3-GFP.

Journal Pre-proof